Charles University

Faculty of Science

Ph.D. study program: Inorganic chemistry

Mgr. Milan Bouša

Preparation and characterization of nanomaterials for electrochemical energy storage
Příprava a charakterizace nanomateriálů pro elektrochemické ukládání energie

Doctoral thesis

Supervisor: Prof. RNDr. Ladislav Kavan, CSc. DSc.

Prague, 2017

Acknowledgements

I would like to express my great thanks to my supervisor Prof. Ladislav Kavan and my consultant Dr. Otakar Frank for kind guidance, a lot of patience and generally for all help. I also thank all my colleagues from the Heyrovsky Institute of Physical Chemistry of the CAS, for the collaboration in such a pleasant and helpful collective. Finally, without huge support from all my friends, beloved girlfriend, and my entire family I would not have been able to finish my thesis and all my studies.

Abstrakt

Výzkum (nejen) uhlíkatých nanomateriálů v čele s grafenem je v současné době jednou z nejčastěji studovaných oblastí materiálové fyziky a chemie, zejména díky mimořádným vlastnostem těchto materiálů vhodným k využití pro konverzi a uchování energie. Během syntézy grafenu a následné manipulace však dochází k narušování jinak téměř ideální krystalové struktury grafenu a tím i ke změně jeho elektronických vlastností. Proto je naprosto nezbytné mít strukturu grafenu „pevně pod kontrolou", čehož je možné dosáhnout pouze vývojem a použitím pokročilých instrumentálních metod.

Grafen může být snadno připraven oxidací a následnou exfoliací grafitu za vzniku tzv. oxidu grafenu. Jedná se o materiál o tloušťce několika málo vrstev grafitu, který má na svém povrchu navázané funkční skupiny obsahující kyslík, které narušují unikátní, sp^2 hybridizovanou síť uhlíkových atomů a tedy i elektronovou strukturu grafenu. Z tohoto důvodu je pro některé aplikace nutné podrobit oxid grafenu alespoň částečné redukci. V první části této práce je detailně studována jeho elektrochemická redukce za pomoci fotoelektronové, infračervené a především Ramanovy spektroskopie. Dosažené výsledky byly dále porovnávány s referenčním neoxidovaným materiálem. Možné využití tohoto procesu je demonstrováno na elektrochemické aktivaci nanokompozitu oxidu grafenu s $LiFePO_4$.

Druhá část práce se zaměřuje na mechanické, jednoosé natahování jedno- a dvouvrstvého grafenu přeneseného na plastický substrát. Při těchto deformacích byly pozorovány změny v elektronové struktuře grafenu pomocí Ramanovy spektroskopie a výsledky interpretovány zejména s přihlédnutím k velikosti domén grafenu, přítomnosti povrchových „anomálií", jako jsou například trhliny a vrásy, nebo změnám vzájemné orientace grafenových vrstvev. K rozlišení přenesené mechanické deformace a dopování náboji (oba vlivy jsou v grafenu běžně přítomny) byla použita vektorová analýza, upravená pro jednoosý tah.

Na závěr byla vyvinuta metoda pro *in-situ* spektroelektrochemii izolovaných dvourozměrných krystalů, které mohou být zároveň kontrolovaně deformovány nezávisle na ostatních vlivech.

Klíčová slova: grafen, Ramanova spektroskopie, spektroelektrochemie.

Abstract

Graphene research is nowadays one of the worldwide most prominent fields of interest in material science due to many extraordinary properties of graphene and related materials. However, the different techniques of synthesis and subsequent handling and/or treatment have a substantial impact on the properties of the graphene and thus a lot of efforts have been focused on developing of the advanced methods for graphene preparation and characterization.

Graphene can be easily produced by oxidation and consequent exfoliation of the bulk graphite; however, resulting graphene oxide needs to be reduced back to graphene-like structure due to partial restoration of sp^2 network. Herein, a detailed study of the structural evolution of the graphene oxide during electrochemical treatment has been performed using X-ray photoelectron, Raman and infrared spectroscopies and the results were compared with non-oxidized graphene nano-platelets. Additionally, graphene oxide in composite with $LiFePO_4$ olivine material, which is electrochemically almost inactive in a freshly made state, has been tested by repeated electrochemical cycling. Using various electrochemical methods, the progressive electrochemical activity enhancement has been observed and spontaneous graphene reduction was identified as responsible for this phenomenon.

The second part of this work deals with mono- and bilayer graphene under uniaxial in plane loading. Generally, strain and even doping are present in graphene simultaneously and both play an important role in the changes of its electronic structure. The behavior of various strained graphene samples transferred onto the target polymer substrates were examined by Raman spectroscopy and discussed with respect to presence of cracks, wrinkles, grain boundaries and loss of bilayer lattice periodicity. Further, the level of stress and doping transferred to the crystal from the substrate was calculated by the vector analysis method with a specific adjustment for the uniaxial strain.

Finally, a new method for spectroelectrochemical characterization of isolated strained 2D crystals has been established.

Key words: graphene, Raman spectroscopy, spectroelectrochemistry

Table of contents

1 Introduction

In this work, various nanomaterials have been investigated from the perspective of basic research on advanced nanocomposites for optoelectronic and energy applications. In general, graphene, as well as other carbon allotropes, and diverse inorganic oxides play an important role in present/future energy conversion and storage. For example, graphene oxide is nowadays tested for use in solar cells as an electron carrier and used for photocatalysis and electrocatalysis. Graphene with its unique and fascinating mechanical and electronic properties is the ideal candidate for hi-tech technologies, including high yield sun-harvesting and non-silicon electronics. To make these technologies available, it is crucial to understand all principles and processes taking place in these materials and, above all, it is necessary to be able to characterize those using appropriate state-of-the-art instrumental methods.

In the first part, fundamental facts as well as the most important methods of preparation and characterization of nanomaterials used within this work will be summarized.

1.1 Carbon allotropes

It is well known that carbon has many modifications, the so-called carbon allotropes. Various structures are formed due to different configurations of electrons in the valence band of the carbon atom. The allotropes differ in the amount of sp^1 (α,β-carbyne $(C\equiv C)_n$, chaoite), sp^2 (fullerenes, nanotubes, graphene) and sp^3 (diamond) bonded carbon atoms. Furthermore, materials like amorphous carbon consist of a mixture of carbon atoms with varying hybridization. Some of those allotropes can fit in the "nanomaterial" definition, usually in all three dimensions (the usual definition of nanomaterials says that at least one its dimension should be smaller than 10^{-7} m). Nanomaterials in general exhibit unique properties compared to bulk materials primarily due to quantum confinement effects. This is naturally valid also for carbon nanostructures. In this thesis, mainly graphene-related nanomaterials will be discussed.
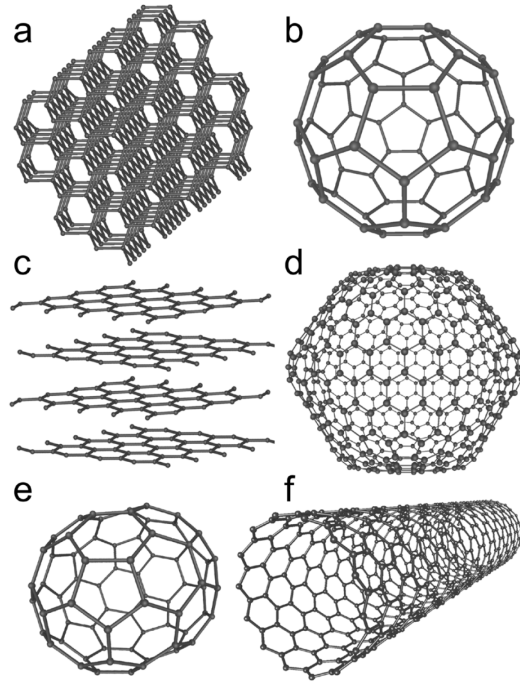
Figure 1: Allotropes of sp^2 hybridized carbon: (a) graphite, (b) buckminsterfullerene, (c) graphene sheets, (d) fullerene C540, (e) fullerene C70, (f) single-walled carbon nanotube (picture under CC BY-SA 3.0 license).

1.2 Graphene

For a long time it was presumed that graphene cannot exist free-standing (isolated), only until 2004 when single-layer graphene was isolated and characterized by nearly a coincidence using adhesive Scotch tape and bulk graphite (HOPG – highly oriented pyrolytic graphite) for mechanical cleavage and subsequent on-tape transferring onto the Si/SiO$_2$ wafer [1]. This method, exfoliation - in adjusted form, is still utilized for laboratory preparation of individual graphene flakes for particular experiments where high-quality defect-free specimens are needed. Since 2004 graphene became one of most scientifically studied materials because of its remarkable properties and promising future use in new industrial and hi-tech fields such as medicine, catalysis, photovoltaics, opto-electronics, advanced transistors fabrication, detectors, sensors and other electronics, energy conversion and storage, or building/transport composites. Graphene is the basic building block of all sp^2 bonded carbon allotropes and can be imagined as "packed" into fullerene (with pentagons added into the

otherwise hexagonal lattice), rolled-up into the nanotubes or stacked to form graphitic structure. As mentioned above, graphene has many unique properties. It is visible by a naked eye, in spite of having 97.7% optical transmittance. It has the highest Young´s modulus of approximately 1 TPa, strength over 160 GPa [2]. Graphene has also the highest known thermal conductivity of ~5000 $W.m^{-1}.K^{-1}$ [3]. Similarly to the case of carbon nanotubes, graphene nano-ribbons (long narrow graphene strips) can be considered as 1-dimensional in term of quantum confinement and they exhibit electronic (semiconducting or metallic) and mechanical properties corresponding to the edge-atom structure type, armchair or zigzag.

It should be noted that the term graphene is not used solely for monoatomic layers. Bi-layer graphene is a stack of two sheets where half of the atoms of the first layer is geometrically aligned in the centre of carbon hexagons of the second layer (AB or Bernal stacking), in some specific cases the carbon atoms of both layers are exactly aligned on top of each other (AA stacking). However, the latter configuration is energetically less favorable, hence much less common compared to the AB stacking. Three and more layers can be aligned in ABA or ABC stacking. Twisted graphene is a general term for bi- or few-layer graphene with misoriented (rotational) stacking. With mismatch angle between the layers, a superlattice is formed, manifested as Moiré pattern. Such structures can be found at the surface layers of natural graphite and also can be prepared in laboratory [4-6].

1.2.1 Graphene oxide

Long time before the first preparation of pristine graphene, graphite oxide, prepared by oxidation (and intercalation) of graphite, and consisting of stacked individual graphene oxide sheets, was known [7]. The oxidation protocol was altered many times, and currently, natural or synthetic graphite is usually used as a starting material and it is oxidized by modified Hummer's method [8], originally using concentrated sulfuric acid, sodium nitrate and potassium manganate, followed by an ultrasonic exfoliation to form graphene oxide (GO), in most cases in the form of water suspension. The resulting GO usually consists of several graphene layers and contains oxidic functional groups, which make GO more suspendable in polar solvents but decrease its conductivity due to the depletion in the conjugated sp^2 network, from the defects created in the otherwise perfect crystal lattice [9].
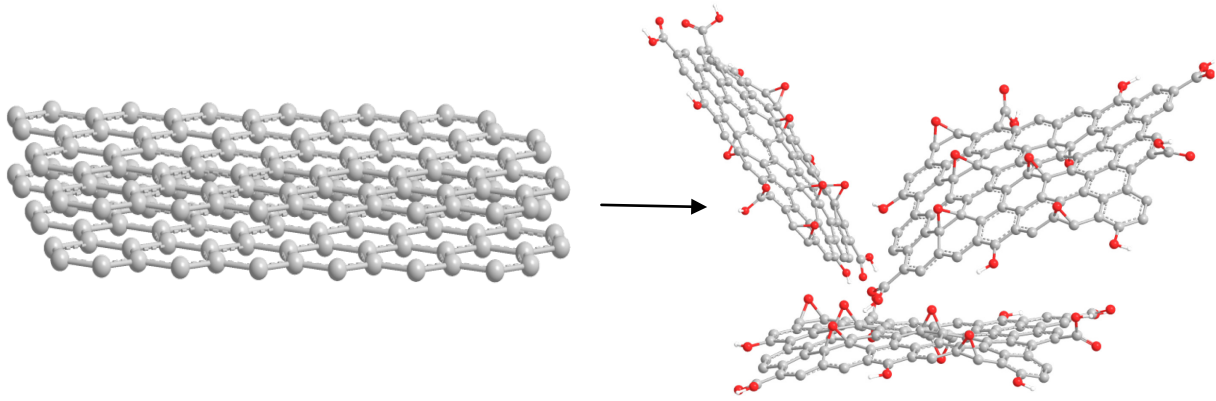
Figure 2: Scheme of graphite bulk (left) and graphene oxide created by oxidization and exfoliation (right). Oxidic functional groups are depicted in red color.

Chemical composition of GO is not yet fully described, as it consists of various chemical groups with non-stoichiometric atomic rates [10]. Several models describe the presence of hydroxyl and epoxy functional groups, carbonyl and carboxyl groups, and, also, esters, lactols or tertiary alcohols are also present [11, 12].

To improve the conductivity of the GO, it needs to be partially reduced to so called reduced graphene oxide (rGO, reduced graphene) using a high temperature treatment [13-15] and/or a reducing agent like hydrogen, hydrazine or sodium borohydride [11, 14-16] and also electrochemicaly [17-27]. However, it is not possible to fully reduce GO back to graphene, because some oxidic-groups always remain and the sp^3 defects in the crystal lattice are not completely healed. Despite those disadvantages, efforts to reduce GO are still alive, because it is a very cheap way to mass-produce fillers for various composites and advanced structures of reduced graphene in a lot of fields of science. More detailed study of GO electrochemical reduction using in-situ Raman spectroelectrochemistry is in the Appendix 1.

1.2.2 Graphene preparation

For later use in laboratory or industry there is an important step in deciding on the right way how to prepare graphene with desirable physical properties. Various methods have

been developed. The first method used for single layer graphene preparation was the mechanical exfoliation advanced by Geim and Novoselov [1], which was at the beginning of the Nobel prize awarded research in 2010. The Scotch tape was used for repeated peeling of the HOPG (after previous treatment due to forming the suitable rough surface), the exfoliated thin layers (floating on surface of acetone as mediator liquid) were deposited on Si/SiO_2 wafer and consequently investigated to reveal the famous ballistic transport of electrons in graphene [28]. This method is allowed by the different and much weaker van der Walls forces between parallel layers (energy ~2 eV/nm) compared to interlayer covalent bonds in graphene layer and the force necessary for peeling of two layers is thus only 300 nN/nm^2 [29]. The exfoliating procedure is convenient for the preparation of well defined crystals especially when single crystalline graphite is used. The lateral dimensions of the obtained single and few-layer graphene flakes can reach 1 mm nowadays, with typical sizes on the order of several tens of micrometers. The main disadvantages are relatively small crystal domains and contamination by adhesives from the used tape. Since the first mechanical cleavage, the procedure has been modified and advanced. In our research group, the procedure is as follows. Cleaned (acetone, isopropyl alcohol, methanol, in ultrasound) Si/SiO_2 wafers (additionally treated with O_2 plasma) and/or various plastic bars (for mechanical experiments) were used as the target support material for exfoliated graphene. For the mechanical experiments, the substrates were covered by a thin spincoated layer of organic compounds, e.g. SU-8 (epoxy-based negative photoresist: SU8 2000.5, MicroChem), PMMA (polymethylmethacrylate) or some other polymers to improve surface properties such as adhesion, roughness, optical attributes – optical contrast. Afterwards, natural graphite was repeatedly peeled by the Scotch tape and gently pressed to the prepared substrate. Finally, the samples were treated by high temperature and/or by UV light to cure the spincoated polymers. All other more detailed steps are described in the experimental parts of the attached papers. The obtained graphene layers must be interrogated to reveal the exact number of layers. The most suitable instruments for this purpose are atomic force spectroscopy, optical and electron microscopy and the mostly used Raman spectroscopy. The mechanical exfoliation is also widely used for fabrication of some other 2D materials, e.g. MoS_2 (molybdenite), WSe_2, hexagonal form of boron nitride, etc.
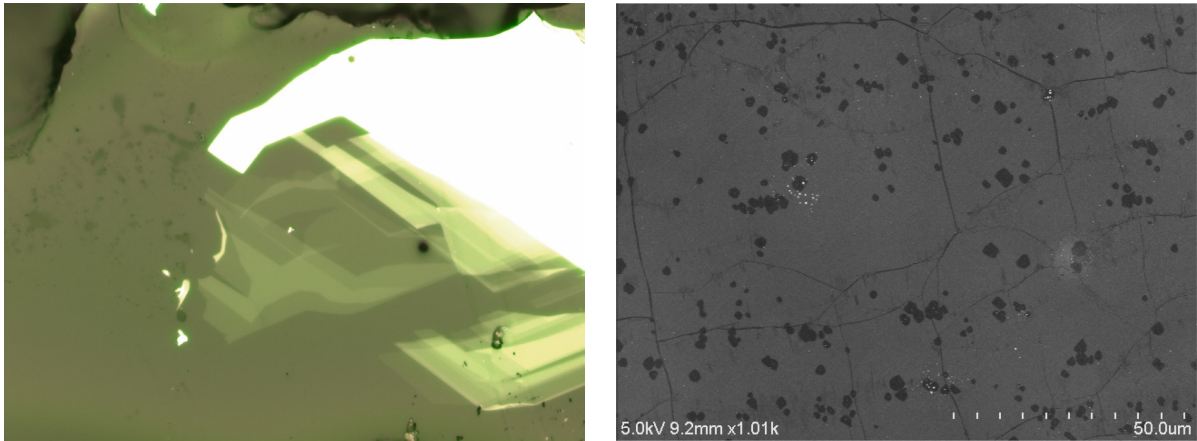
Figure 3: Left: Optical microscope image (mag. 500x) of bulk graphite (lighter part = more layers) and few-layered graphene (varies in optical contrast due to diverse number of layers) as-prepared by mechanical exfoliation. Right: Graphene grown on a polycrystalline copper foil using CVD method. Beginning of the growth of the second layer growth is clearly visible (darker objects), Scanning electron microscope image (mag. 1000x).

Probably the mostly utilized preparation methods for large-area single layers with reasonable quality are "bottom-up" synthesis, especially Chemical Vapor Deposition (CVD) method. The CVD technique is based on the decomposition of carbon precursors as a source for graphene: solid compounds (camphor, PMMA, sucrose, hexachlorbenzene or nanopowder) [30-33], gas precursors (methane, ethylene, acetylene, etc.) [34, 35] or liquid carbon precursors (methanol, ethanol, hexane, etc.) [36-38]. For the purpose of research related to this thesis, catalyst metal (copper foil) was heated up to 1273 K and annealed for 20 minutes under a flow of H_2 in helium, methane was introduced for some specific time (dependent on growth requirements) and finally, the sample was cooled to room temperature. For example, in the case of growing isotopically labeled $^{12/13}C$ double-layer graphene, $^{12}CH_4$ and $^{13}CH_4$ can be injected into CVD system separately [39]. Nowadays, the CVD process can be optimized to yield graphene with single crystal domains with lateral sizes in mm range, and possibly even larger ones on metal catalysts with uniform single crystalline surface, with controlled number of layers. However, due to the need of a metal catalyst, it is necessary to subsequently transfer the as-grown graphene to a desired substrate; unfortunately, this process involves the formation of physical defects as cracks and wrinkles in the graphene crystal.

There are several other approaches how to prepare single or few-layer graphene. Liquid-phase exfoliation produces large amounts of graphene sheets (both single and few-layer) using organic solvents or surfactant-water solutions together with expanded graphite with quite high yields [40-42]. Graphene can be further produced by epitaxial growth on silicon carbide [43], by unzipping of single/double-walled carbon nanotubes or fullerenes [44-46] resulting in high quality nanoribbons or by precipitation from carbon-rich transition metals such as nickel [47].

1.2.3 Transfer techniques

Requirements for substrates needed for the fabrication of nanoscale structures for research and applications often differ from those used for graphene preparation. Especially, CVD method produces large-area graphene films using metal catalysts, and, therefore, it is usually necessary to move graphene onto various different substrates (e.g. plastic sheets for flexible transparent electronics, gate dielectrics for electronic applications). Until today, many transfer procedures were invented, generally involving synthetic polymers as sacrificial support layers during the transfer.

Recently, the most generally utilized method is the wet transfer technique using polymethylmetacrylate (PMMA) as the sacrificial polymer [48], which was frequently used within this thesis as well [49, 50]. In general, a thin polymer layer is spin-coated onto the graphene resting on the metal foil, which is thereafter etched away, e.g. in $FeCl_3$, HCl, $Fe(NO_3)_3$, or $CuCl_2$ solutions. The graphene-polymer stack is washed in deionized (D.I.) water and left floating on the water surface. The whole stack is than picked-up by the target substrate, and finally PMMA is dissolved in an appropriate solvent (most usually in acetone or acetone vapor) and/or cleaned thermally (~300°C). While this method is simple and capable of transferring large-area samples, there are several disadvantages. Firstly, PMMA reacts slightly with the metal etchants leaving unwanted residues on graphene [51]. Secondly, the "fishing" method is inappropriate for transferring onto hydrophobic substrates, and, finally, some applications require polymeric substrates, hence the final step of support polymer dissolution/annealing has to be modified in order not to damage the target polymer. An alternative solution of different polymer than PMMA, which could be soluble in less

aggressive solvents (short aliphatic or alicyclic hydrocarbons or alcohols) could be an advantage for some purposes. In this way, the problems with PMMA residues can be solved simultaneously [51]. For example, transfer using acetic acid, instead of acetone for post-transfer sample cleaning, was described as preferable due to avoiding of the polymer residues usually identified in common treated samples [52]. Processes without using the sacrificial polymer were also documented [53]. The authors used a mixture of isopropyl alcohol (IPA) and ammonium persulfate [$(NH_4)_2S_2O_8$] solution as etchant. After dissolving the metal, single layer graphene remains floating on the surface. The solution was then exchanged for a mixture of D.I. water and IPA to achieve the required surface tension. The fished out graphene is then polymer-remnants free [52].

Moreover, some other polymers were found suitable for graphene transfer. The main advantages of cyclododecane ($C_{12}H_{24,}$ CDD) are its solubility in non-polar and aromatic compounds, hydrophobicity and sublimation under room conditions. It is therefore possible to treat the sample by heating to remove nearly all CDD residues [54]. Another available carrier material is poly[$_L$-lactic acid] (PLLA) [55], with which 2D materials can be easily transferred onto both hydrophobic and hydrophilic surfaces via PLLA polymer attached to a glass slide. A droplet of water penetrating preferentially between hydrophobic polymer (with the attached 2D material) and hydrophilic initial substrate (Si/SiO_2) cause their separation. Primarily, mechanically exfoliated materials are convenient for PLLA transfer process [56].

Instead of the wet transfer, which is not the proper method for hydrophobic target substrates, some dry transfer method can be used. For several experiments in thesis-enclosed papers we used dry "stamping" procedure where a chunk of poly(dimethylsiloxane), PDMS, is placed on the graphene/sacrificial polymer (spincoated polyisobutylene, PIB) stack before the metal-etching and the stamp is peeled off mechanically after the placement onto the target substrate (see Fig. 4). The final step is to remove the support polymer layer, hexane is used in the case of PIB [57].
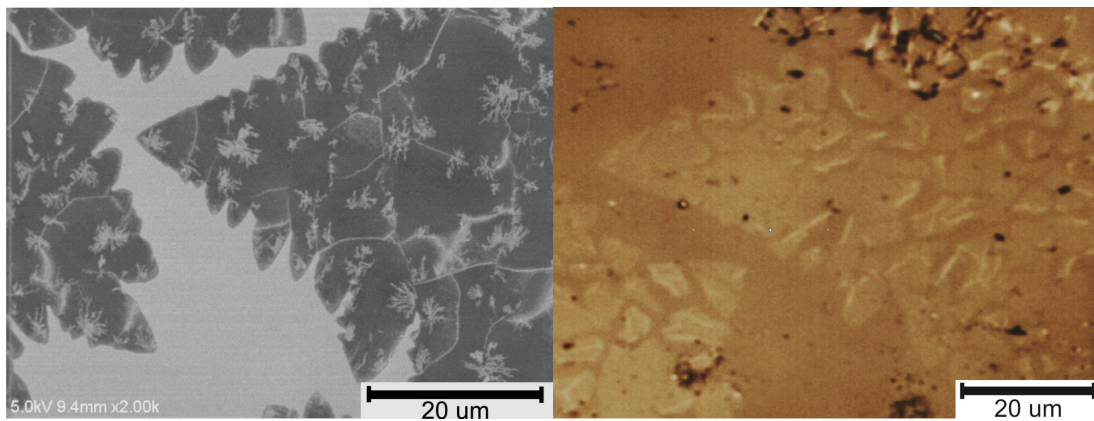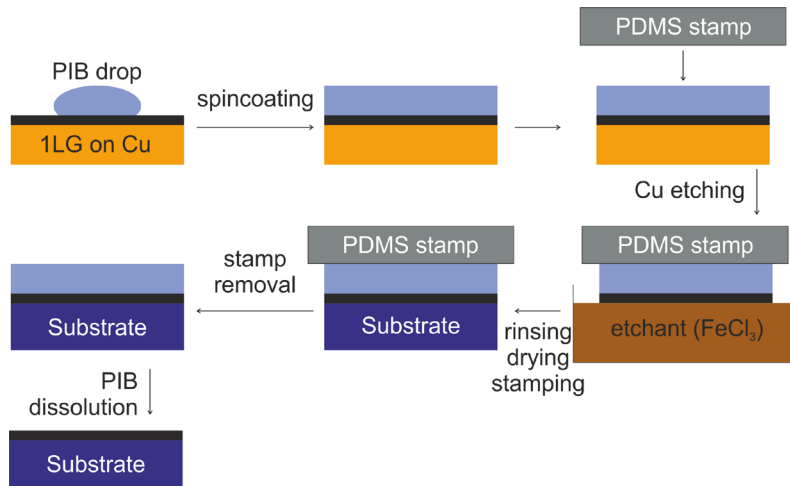
Figure 4: Top: PIB assisted "dry" transfer technique procedure scheme. Bottom: Comparison of mono-layer graphene before (as prepared on copper, SEM image, left) and after PIB assisted transfer (on PMMA bar, optical image, right)

Thermal-release tapes can be also used for transfer, but its price is too high to be used commercially on a large scale at the moment [58]. More exotic transfer methods include for example the direct lamination of CVD graphene from copper onto various flexible substrates in a pressing device [59], or micro-transfer contact printing [60] onto gold-coated Si/SiO$_2$ using graphene as "ink". All mentioned transfer techniques involve benefits (scale, purity, price etc.) as well as some problems (deformation, used chemicals), so it is crucial to pick the proper one for the desired application and also to optimize the protocol according to the required properties of graphene structures and target substrates.

1.2.4 Electronic structure in graphene

Pristine (single-layer) graphene is one atom-thick sheet of carbon atoms that are packed in a hexagonal honeycomb crystal lattice and could be casually described as a one single layer of sp^2 bonded carbon atoms in graphite. Every atom, except for those on the edges, in an ideal graphene has three σ-bonds (2s, 2p$_x$ and 2p$_y$ hybridized orbitals, average distance between carbon atoms is 1.42 Å [61]) with the nearest surrounding atoms, and one π-bond (2p$_z$ orbital) oriented perpendicularly out of the 2D crystal plane. Those π-orbitals in all graphene carbon atoms form conjugated hybridized π (bonding) and π* (anti-bonding) bands and are the cause for the peculiar electronic properties such as extremely high charge mobilities even at room temperature [62], thermal conductivity 5000 W m^{-1} K^{-1} [3], etc.

Graphene has a linear dispersion of electrons and holes (forming the Dirac coins), thus the valence and the conduction bands are "touching" in the Dirac points (non-equivalent K and K´ points in reciprocal space, see Fig. 5) making graphene a zero band gap semiconductor (semimetal). As mentioned, in the armchair type of graphene nanoribbons there is a difference; the band gap has a finite energy in there. In the graphene Brillouin zone (primitive cell in reciprocal space, BZ) there are three (four with K´) points of high symmetry, namely Γ, K and M in the centre, on the corner and in the centre of the edge of the hexagon-shaped primitive cell, respectively.

According to calculations, energy of the σ bands is far away from the Fermi level [63], however, this does not apply to π bands (Fig. 5, bottom). Two electrons are in the π band which leaves π* unoccupied, and those bands are hybridized in K (K´) symmetry points. Presence of the Fermi level precisely in those K points is due to the equivalency of the carbon atoms in BZ. There are, again, two atoms in the unit cell and therefore six normal modes around the Γ point with two of them doubly degenerate. E$_{2g}$, one-degenerate in-plane optical mode is active in the Raman process (RP).
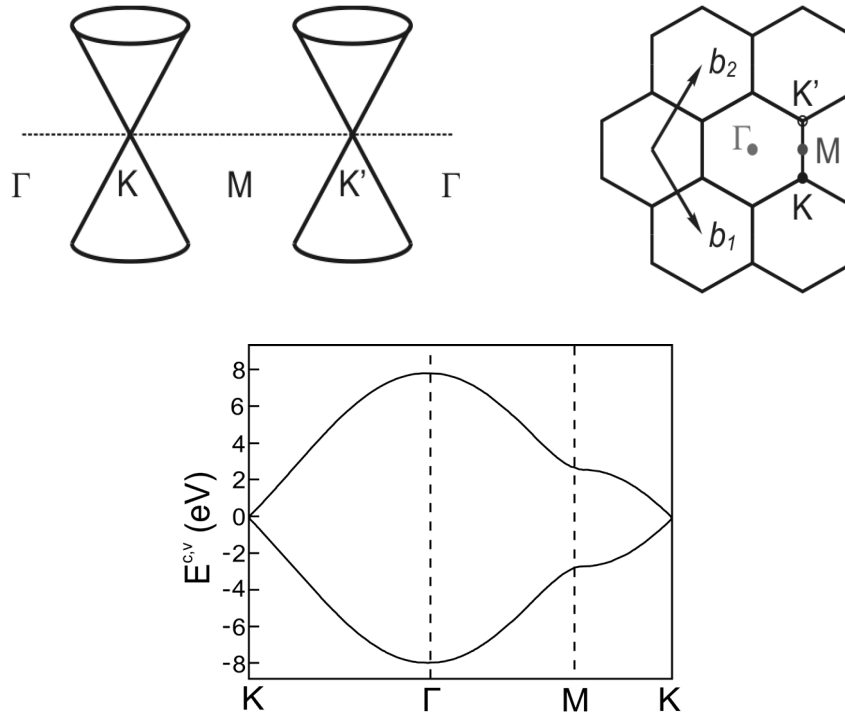
Figure 5: Left: Scheme of a graphene projected in 2D reciprocal space with the distinctive Dirac cones and Fermi level (dotted line). Right: Marked reciprocal lattice vectors (b1, b2) and points of high symmetry (K, K′, M, Γ), in graphene Brillouin zone (hexagon in the centre). Bottom: Energy dispersion for π and π* bands along the high symmetry points (Fermi level is zero in K points). Bottom picture adapted with permission from Taylor & Francis from Ref. [63].

By adding the second graphene layer to form bi-layer graphene, the electronic structure changes. The π and π* orbitals split into symmetric and antisymmetric combinations resulting in a quadratic electron dispersion instead of the linear one [64]. Moreover, two parabolically dispersed bands are introduced. These bands, π_1 and π_1*, do not touch in the Dirac point this time.

1.2.5 Raman spectroscopy of graphene related materials

Raman spectroscopy is one of the preferred methods for the characterization of carbonaceous materials. It is fast, non-destructive and very sensitive to changes in the

structure of these materials. It can provide information about the electronic structure of graphene, number of layers [65], interlayer coupling [66], structural defects [26, 67], or chemical functionalization. Moreover, phonons (and thus Raman peaks) react to magnetic field, temperature, stress/strain and doping [49, 68, 69] and many other physical or chemical stimuli.

In a simplified view, the Raman effect is based on the interaction of a photon with molecular vibrations. In the resonant Raman effect, additional interactions with charge carriers - in general with an exciton (electron - hole pair) of energy equal to the energy of the incident photon - take place. The incident photon can pass through the material or can be absorbed, reflected or photoluminescence can appear. Further, when interacting with atoms or molecules the photons can be scattered elastically (Rayleigh scattering) or, in very few cases ($\sim 10^{-7}$ photons), the photon can interact with a specific vibration of the molecule in such a way that the molecule is excited to a virtual energy state. When the photon is released back, its energy is different compared to the initial one. The resulting energy of such an inelastically scattered photon can be lower or higher (Stokes and anti-Stokes shift) and those shifts, i.e. difference between energy of the incoming and outgoing photon, appear as bands in the Raman signal. Usually, only Stokes processes are studied by Raman spectroscopy and therefore displayed in spectra. To have an active Raman transition there must be a change in the electric dipole polarizability of the molecule during the vibration.

For a better understanding of the Raman scattering in sp^2 carbons it is important to describe phonon (vibrational quantum of energy) dispersion in graphene. Its unit cell consists of two unequal carbon atoms and therefore there can be calculated six phonon dispersion bands labeled oTA, iTA, iLA, oTO, iTO, iLO. Three branches are acoustic (A), three optic (O). Two bands have their origin in vibrations perpendicular to the graphene plane (out-of-plane phonons, o) and for the other four, the phonons modes are in-plane (i). If the nearest C-C atoms bond is taken as basic direction, than phonon modes could be denoted as longitudinal (L) and transverse (T) when the vibration is parallel or perpendicular, respectively. All six phonon branches are showed in Fig. 6 in graphene 2D reciprocal space [63].
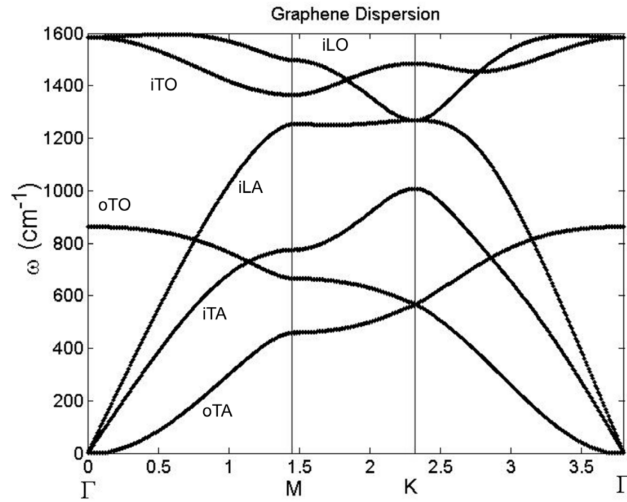
Figure 6: Calculated phonon dispersion curves for mono-layer graphene. Energy (as relative reciprocal centimeters) is plotted against high symmetry points in Brillouin zone (oTA, iTA, iLA, oTO, iTO, iLO). Adapted with permission from American Physical Society from Ref. [70].

Concerning the number of scattering events in the Raman process, the order of the RP can be distinguished. In the first order process one phonon with a very small momentum is created. Double resonant processes can involve one or two phonons during two scattering events and shows overtones (multiples of integers for Raman modes) and combination modes (in the Raman spectra, they appear as sum of different phonon induced modes). The Raman spectrum of graphene shows numerous peaks, including those common for all carbonaceous materials. Nevertheless, in most cases, only two to four main Raman features are usually considered and evaluated.

The G mode (so called "graphitic", usually around 1580 cm^{-1} for suspended graphene) assigned to the E_{2g} symmetry high frequency phonon at the Γ point is common for all sp^2 bonded carbon allotropes. It is a first order, doubly degenerate (optical transverse iTO and longitudinal LO) phonon mode caused by the vibration of carbon atoms in plane [71]. It does not require the whole carbon hexagons, but appears in every sp^2 bonded area. G band is sensitive to hydrostatic pressure and both uniaxial and biaxial strain as well. In general, tension induces redshift (also known as band downshift / softening, i.e. shift of a band position to lower numbers of cm^{-1} on the x-axis in the Raman spectra), while compression

induces blueshift (i.e., upshift / phonon stiffening).On top of that, uniaxial strain causes splitting of this band into G^+ and G^- subpeaks. The splitting takes place due to different atomic motions parallel or perpendicular to the direction of the induced strain. The G band is also very sensitive to doping (hole or electron). The effects of strain and doping, together with their disentangling from the Raman spectra will be discussed more detailed in the next chapters. There are other stimuli, which inflict changes in the G band characteristics (Raman shift, linewidth, intensity), e.g. increasing temperature red shifts the G band. However, within this thesis, the temperature effect is taken into account only to the extent of not overheating the sample during measurement (in other words, the laser power is always kept low enough not only to avoid the sample damage, but also to prevent unwanted shifts from the local heating).
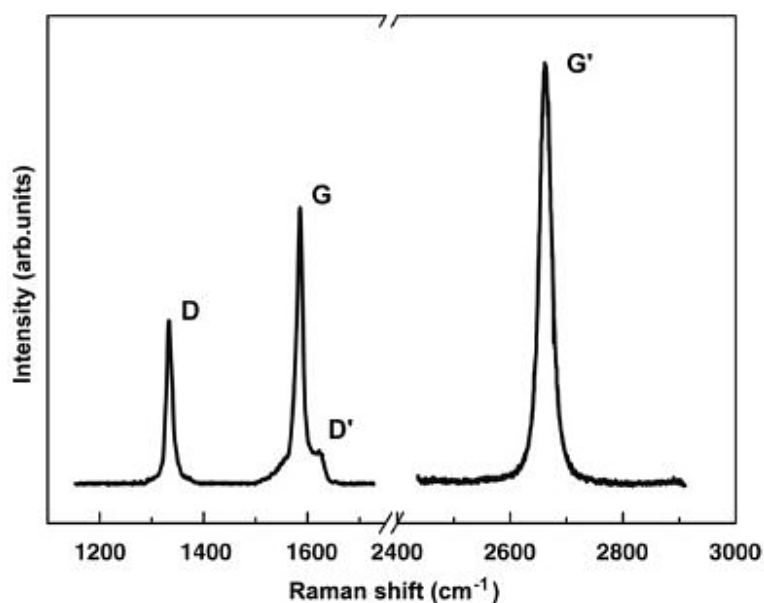
Figure 7: Typical Raman spectra of defective graphene with three prominent peaks: D, G(+D′), G′ (also called 2D). Adapted with permission from Elsevier from Ref. [64].

D (intravalley, ~1350 cm^{-1}) an d D' (intervalley, ~1615 cm^{-1}) modes are induced by the presence of defects in the hexagonal graphitic structure. An electron from the valence band is inelastically scattered by a phonon and elastically scattered by the defect upon D band generation. It is a second order double resonant process between K and K′ points

demanding one phonon (iTO) and a defect [72]. This mode appears only in the defective sp^2 carbons, it is not present in perfect graphene. The D mode (as are also the D′ and 2D modes) is dispersive, its position and intensity change with the photon energy (for E_{laser} = 2.41 eV, the frequency, ω = 1350 cm^{-1}). The D band shift change and also linewidths (usually evaluated as full width at half maximum, FWHM) can be used for the estimation and description of disorder (with information obtained from other methods taken into consideration, see Ref. [26]). Sometimes, Tuinstra-Koenig relation is being used for calculating the lateral domain size (L_a) in graphene using the ratio of D and G intensities {I(D)/I(G)} [71].

$$\frac{I(D)}{I(G)} = \frac{C(\lambda)}{L_a}$$

Equation 1: Tuinstra-Koenig equation [C(λ) is excitation-dependent proportionality constant].

The 2D band (in literature also as G′, ~2500-2800 cm^{-1}) is approximately twice the frequency of the D mode, the D band overtone, but is not connected with any disorder. It is generated by the second-order (intervalley) double- or triple-resonant process between the K and K' points involving two phonons. As mentioned above, the 2D mode is energy dispersive. The 2D peak attributes again respond to the changes of strain and doping but in a different manner compared to the G mode. Using the 2D mode, it is possible to study additional properties of the system, e.g., the number of layers and their stacking order - the 2D mode in single layer graphene can be considered as a single Lorentzian lineshape, but the Bernal stacked bi-layer graphene exhibits the 2D mode consisting of four Lorentzian peaks. Also, the intensity of the 2D band is the highest for one layer only (owing to the triply resonant character in this particular case).

Many others Raman bands can be observed in the spectra of graphene or in graphitic materials in general. Briefly: D′′ (~1500 cm^{-1}), 2D′ (overtone to D′, ~3240 cm^{-1}) [73], combined modes (e.g. two phonon induced D + D′) [65] or some more exotic bands such as the R modes (rotational, one phonon processes due to the structure modulation without requiring defects) observed in twisted multilayered graphene and which depend on the mismatch angle between the two superposed layers [4]. In this work, in particular the D, G

and 2D bands are essential, thus Fig. 8 illustrates schematically the processes underlying these modes as displayed in the reciprocal space.
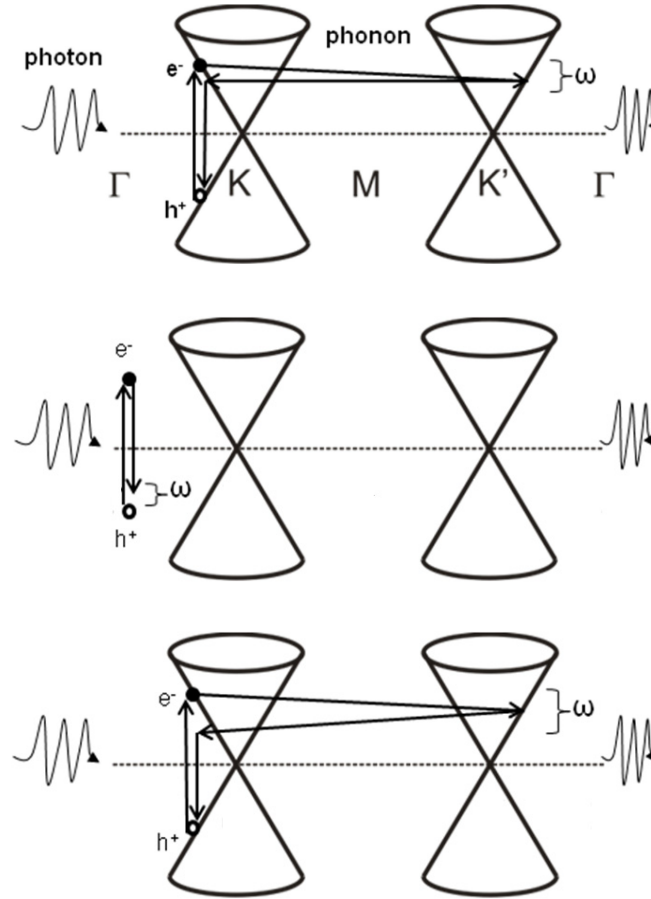
Figure 8: Graphic illustration of one-phonon second-order double resonance D mode (top), first order doubly degenerate G mode (middle) and two-phonon second-order double resonance G´(2D) mode (bottom). Generated Raman shift: ω, Fermi level: horizontal dashed line.

Due to isotope labeling, there is a great chance to examine fundamental properties of multi-layer graphene samples when different layers are fabricated by the CVD method using isotopically differentiated precursors [69]. The isotope-induced shift between the ^{12}C and ^{13}C graphene bands of the same origin can be expressed as in the Eq. 2.

$$\Delta_{12-13} = \frac{\omega_{12} - \omega_{13}}{\omega_{12}} = 1 - \sqrt{\frac{12 + c_0^{13}}{12 + c_{13}^{13}}}$$

Equation 2: All-carbon vibrations isotope shift calculation (ω: Raman peaks position; c_0^{13}: concentration of ^{13}C isotope naturally present in ^{12}C sample; c_{13}^{13}: concentration of ^{13}C isotope in enriched sample).

1.2.6 Strain and doping in graphene

It is well known that one single layer of the graphene has a zero bandgap under standard conditions. The bandgap could be "opened" by several ways, for example by pattering of the graphene 2D structures [74], using special substrates or by temperature induced strain [47, 75]. Applying the uniaxial tensile strain or better the combination of uniaxial and sheer strain - considering the calculated very high strain levels needed in the first case, bandgap can be engineered and opened. However, the necessary strain is still quite high (up to 18%) to be obtained and used in practical applications [76]. The bandgap engineering by mechanical deformation can have a huge impact on the use of graphene in nanoelectronics or, for example, as a part of prospective flexible solar cells. As shown also by our Raman spectroscopic study of bilayer graphene under uniaxial tension (Appendix 3), Raman spectroscopy can be indeed a very useful characterization technique not only to determine the basic properties of graphene, but also a plethora of more advanced characteristics and to serve as a direct probe of the graphene electronic structure.

As mentioned in the previous sub-chapter, tension causes phonon softening due to the lowering of the lattice energy (decrease of the interaction forces between atoms), and thus the Raman bands are redshifted [77]. Compression produces the exactly opposite effect, blueshift. Under uniaxial strain, the G peak splits into two components G^+ (perpendicular to the strain axis) and G^- (parallel with the strain axis) with shift rates of ~10-14 and ~30-33 cm^{-1}/%, respectively, for graphene on polymer substrates. The response to tension/compression is not only reflected in the sign if the peak shift changes, but also in their overall behavior: under tension the peak frequency changes follow linear trends, while under compression the evolution of the peak shifts follows a second order polynomial due to progressive buckling of

the layer [78]. Under uniaxial strain, the 2D mode splitting was observed too, but the character of the splitting depends on the direction of both the applied stress and polarization of incoming light with respect to the crystal lattice orientation in the reciprocal space, namely of the K-K' pairs [79]. Shift rates for biaxial strain are also reported for G and 2D bands, and they are more than twice the shifts induced by the uniaxial strain [80]. For our purposes of mechanical uniaxial deformation of graphene (Appendices 3 and 4), cantilever beam technique was used together with in-situ Raman spectroscopy (Fig. 9).
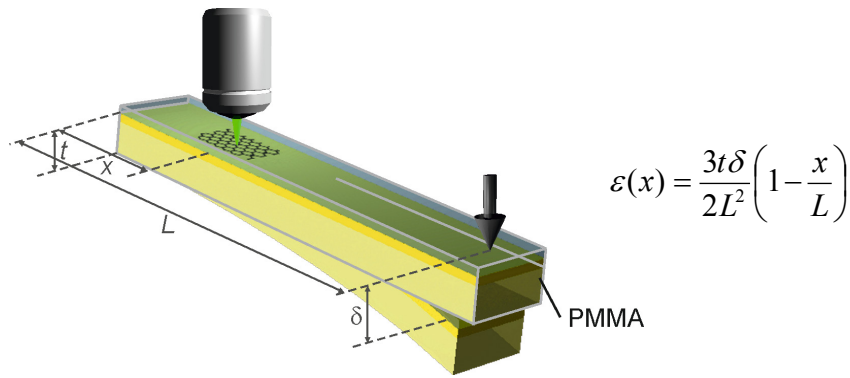

$$\varepsilon(x) = \frac{3t\delta}{2L^2}\left(1 - \frac{x}{L}\right)$$

Figure 9: Scheme of the cantilever beam experimental setup and equation for the nominal strain $\varepsilon(x)$ calculation on the top of the beam (i.e. in the graphene) on the investigated spot. The downward bending direction marked by an arrow induces uniaxial tension.

Doping of graphene can be understood either as an injection of electrons into the conduction band (n-type doping) or as a depletion of electrons (injection of holes) from (to) valence band (p-type doping) causing shift of the Fermi level. Frequency of the Raman G band increases even with small doping levels regardless of the doping type. Electron doping causes only insignificant shifts of 2D frequencies for the concentration of electrons e $\leq$ 2 x 10^{13} cm^{-2} and beyond that a non-linear softening for progressive n-doping [81]. Hole doping shifts the 2D band position to higher wavenumbers, however, not linearly. Both doping directions decrease FWHM of the G and increase FWHM of the 2D bands [49, 65, 72, 82].

The precise distinction between doping and strain, both usually present and distributed throughout each graphene flake, is of utmost importance. In Appendix 4, a useful method

(modified for uniaxial strain) for doping vs. strain separation via vector analysis of in-situ Raman data sets is presented.

1.3 LiFePO$_4$ olivine

LiFePO$_4$ (LFP, olivine family mineral triphylite) is considered a promising cathode material in Li-Ion batteries [83, 84]. During charging of LFP, the lithium ions are extracted from its structure into the electrolyte. In the discharge process, lithium ions are inserted back. The main advantages of LFP are its flat voltage profile, low material cost, sufficient material supply, high stability and better environmental compatibility compared to other cathode materials. LFP has a theoretical capacity of 170 mAh/g however, the strong covalent bonds between oxygen and phosphorous or iron also lead to low ionic diffusivity and poor electronic conductivity, therefore the real capacity of pristine LFP is insufficiently low.
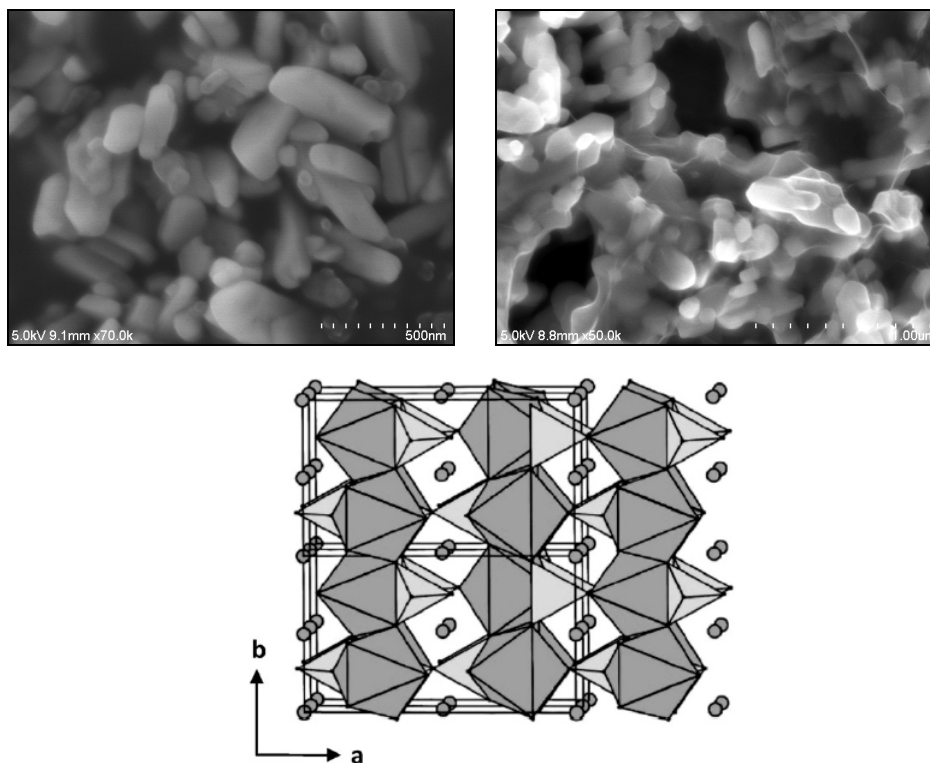
Figure 10: SEM image of pristine LFP crystals (left) and mixture LFP/GO (right). The crystal structure of pristine LFP viewed along the c-axis (bottom). Iron atoms occupy octahedral sites (dark shaded), phosphorus atom tetrahedral sites (light shaded). Lithium atoms are depicted as small circles in octahedral positions. Adapted with permission from Elsevier from Ref. [85].

LFP conductivity thus needs to be improved, and it can be done for example by decreasing the crystal size (enlargement of active surface), doping, carbon coating [86] or addition of some type of conductive carbon such as carbon black, graphene oxide or carbon nanotubes [27, 87, 88]. Electrochemical activation of LFP by simultaneous reduction of graphene oxide is studied in-situ and described in Appendix 2.

2 Aims of the thesis

With respect to the previous work of the research group of Prof. Ladislav Kavan at the J. Heyrovsky Institute of Physical Chemistry of the CAS, the work has been aimed on the selected aspects of preparation and characterization of nanomaterials for electrochemical energy conversion and storage. In spite of the seemingly too broad nature of the studies, there were two strong links connecting them: (i) graphene, in one form or another, as an important building block of the nanocomposite, and (ii) the use of advanced in-situ Raman spectroscopy techniques to investigate the behavior of the materials relevant to the possible application.

The results, which are incorporated in the attached papers, can be organized into two main chapters. In the first one, electrochemical reduction of graphene oxide was studied by Raman microspectroscopy, and, furthermore, for the GO/LFP composite, a specific case (reduction or activation for GO and LFP, respectively) of rGO utilization in cathodic battery material was tested.

The second area of research in this work consisted of systematic Raman studies of mono- and bi-layer graphene under uniaxial in-plane loading which is important in terms of potential utilization of graphene as a component of flexible photovoltaic devices. Several angles of the graphene and its interface to a polymer substrate were examined: the comparison of behavior of strained mono- and bilayer graphene, the effect of cracks, grain boundaries and delaminated wrinkles on the interfacial shear stress transfer, the effect of the loss of periodicity in bilayer graphene, and, from a fundamental methodological point of view, the separation and quantification of both the strain and doping levels by modified vector analysis of Raman data sets.

As a final target, development of an advanced spectroscopic method combining in-situ doping and strain loading was chosen.

3 Concise summaries of results and discussion

3.1 Raman spectroelectrochemistry of graphene oxide

3.1.1 Electrochemical reduction of graphene oxide

As mentioned earlier, graphene oxide (GO) is heavily decorated by various oxidic functional groups introduced during the GO fabrication, which makes the material more soluble in polar solvents, but substantially decreases its conductivity. For this reason, GO needs to be reduced to repair the sp^2 network at least to some extent. One of the possible, simple and effective, ways of GO reduction is an electrochemical treatment, for example by spontaneous self-activation as a constituent part of a nanocomposite material of electrochemically cycled cathode for secondary lithium-ion batteries.
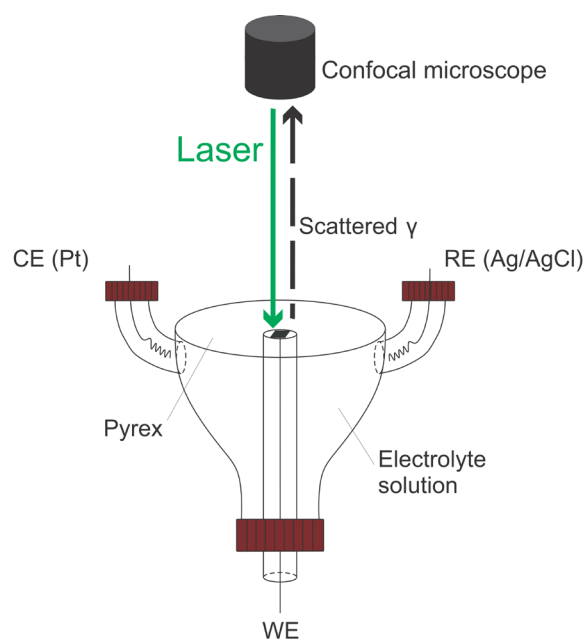

Figure 11: Schematic illustration of the three-electrode cell used for Raman SECH measurements, electrodes labeled as used in protic solvent case. (RE: reference electrode; CE: counter electrode; WE: working electrode). Sample on platinum mesh depicted as a black rhomboid under the laser beam spot.

Few Layered Graphene Oxide (FLGO; 2-4 layers, thickness <3 nm, avg. dimensions of individual flakes 300-800 nm) and Graphene NanoPlatelets (GNP; thickness <3 nm, avg. diameter 5μm) were both suspended in D.I. water (1 mg/mL) or isopropanol (IPA), respectively. The suspension was doctor bladed onto F-doped SnO_2 conducting glass support and left to dry under room conditions. For experiments in aprotic electrolyte solutions, the material was mixed with 5 wt% of polyvinylidene fluoride (PVDF) dissolved in N-methyl-2-pyrrolidone (NMP), and doctor bladed the same way (area of the films ~1 cm^2). Finally, the electrodes were dried at 100°C in vacuum. Electrodes for in-situ Raman spectroelectrochemistry (SECH) consist of only dip-coated FLGO (or GNP) on the platinum mesh (99.9% purity). The schematic illustration of the SECH cell is in Fig. 11. For aprotic environment the electrolyte solution was 1 M $LiPF_6$ in ethylene carbonate + dimethylcarbonate (EC/DMC; 1/1; w/w). The reference and counter electrodes were from Li-metal, hence all potentials are quoted against the Li/Li$^+$ reference electrode in this medium, and measurements were carried out under Ar atmosphere. During the in-situ Raman SECH, Ag wire as pseudoreference and platinum wire as counter electrodes were used with 1M KOH electrolyte solution.

In Fig. 1 of the Appendix 1, cyclic voltammograms (CV) of FLGO and GNP electrodes are displayed. In the case of the FLGO, reduction peak (~2.4 V vs. Li/Li$^+$) is clearly visible in the first cycle and during the following progressive cycling the peak current decreases. Moreover, the decrease of current densities at the reduction side of the voltammograms is also pronounced. Those changes could be explained by the progressive reduction of some of the attached oxidic groups. No such effect was observed in the GNP voltammograms due to absence of those groups in the initial material.

Another view of those processes can be obtained by X-ray photoelectron spectroscopy (XPS). GO and GNP samples were prepared on a gold foil (99.95% purity) from D.I. water or IPA solutions. XPS peaks C1s and O1s were used for comparing of GNP, original FLGO and FLGO after 70 electrochemical cycles. However, it is very difficult to deconvolute overlapping multi-peaks, thus three subpeaks for C1s and two for O1s bands were fitted. For the C1s peak there is a band assigned to C-C (binding energy 284.6 eV) and two bands for carbon–oxygen functionalities: C-O (hydroxyl and epoxy groups, 286.7 eV) and CO + OC-O$^-$ (288.2 eV) [14, 16]. Two bands are included in O1s peak: CO (O-CO$^-$, 531.1 eV) and C-O (532.6 eV). Two most pronounced changes during cycling can be traced: Firstly, C/O

stoichiometric ratio increases and, secondly, subpeak on 532.6 eV relatively decreases. It is presumed that preferential reduction of functional groups containing less oxygen, and/or evolution of CO_2 could take part upon cycling.

Raman spectra were measured by Labram HR spectrometer (Horiba Jobin-Yvon) interfaced to a microscope with 50x long working distance objective. Spectroelectrochemical in-situ studies used 514 nm (2.41 eV) and ex-situ electrochemistry 514 or 633 nm (1.96 eV) laser excitation. The D and G(+D') peaks were fitted by Lorentzian and Breit-Wigner-Fano (BWF) lineshapes, respectively [67, 89].

$$I(\omega) = \frac{I_0 \left[1 + 2 \frac{(\omega - \omega_0)}{Q\Gamma} \right]^2}{1 + \left[2 \frac{(\omega - \omega_0)}{\Gamma} \right]^2}$$

Equation 3: Breit-Wigner-Fano lineshape equation (I_0: peak intensity; ω_0: peak position; Γ: FWHM of the peak; Q^{-1}: BWF coupling coefficient.

Raman spectroscopy *ex-situ* before and after electrochemical treatment was carried out to probe the impact of the voltammetric cycling on both FLGO and GNP materials. After the 50 voltammetric cycles the I(D)/I(G) ratio increases, the D and G peak positions redshift and FWHM of both bands decreases. Ratio of D and G Raman band intensities, I(D)/I(G), is usually increasing during reduction of GO and is often misunderstood as spontaneous introducing of other defects in the graphene crystal lattice (according to the Tuinstra-Koenig relation, see chapter 1.2.5) and even diminution of graphene lateral domain size. However, it is necessary to take all of the parameter changes into consideration. Narrowing of FWHM of both main peaks clearly points to structural ordering. Downshift of the D band can be explained by increasing the size of the aromatic clusters. Redshift of the G band is unclear and contrary to expectations by Ref. [67], and it could be connected with changes of both subpeaks (G and D') parameters whose response on reduction could be independent. Therefore, it is necessary to explain increasing I(D)/I(G) parameter upon the reduction by a different model, and it can be done using the "amorfization trajectory model" first introduced in Ref. [67]. During amorfization in the stage 2 (NC-Graphite → amorphous carbon, Fig. 12,

orange arrow) average distance between the defects is increasing due to opening of the aromatic rings and I(D)/I(G) parameter here depends on the second power of L_a (lateral domain size) [67]. Increasing of the I(D)/I(G) of FLGO is thus in good agreement with all other changes upon reduction. The electrochemical cycling of GNP is reflected in changes in presumed direction (Fig. 12, red arrow).
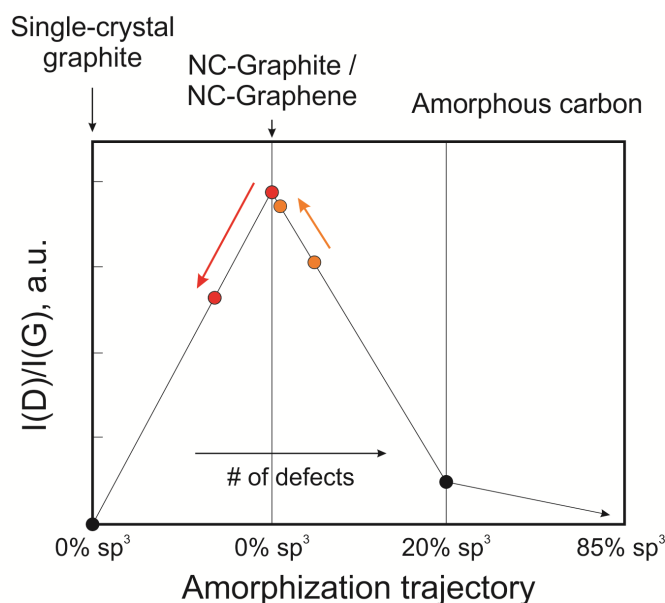
Figure 12: Modified amorfization trajectories diagram [67]. I(D)/I(G) parameter changes upon reduction of FLGO and GNP are marked by orange or red arrow, respectively.

In-situ Raman spectroelectrochemistry was performed to examine the reversibility of GO/GNP oxidation/reduction under electrochemical treatment, both short- and long-term (Fig. 5 and 6, Appendix 1). GNP spectra show nearly reversible behavior with only small changes in the observed parameters, probably caused by mild redox process and/or lattice contraction/expansion due to doping. The FLGO behavior can be divided into two main phases, the first of which is different to GNP. In this phase, reduction of FLGO, due to relatively fast cutting-off the oxidic groups, is strong. The second phase is mostly reversible, however, small differences between oxidation and reduction of FLGO still can be observed.

3.1.2 Activation of graphene oxide/LiFePO$_4$ olivine composite

The practical consequence of the effects described above can be demonstrated in the case of LFP/FLGO composite, which is electrochemically almost passive in a freshly made state and spontaneously enhances its activity when the electrochemical charge/discharge cycling progresses. To demonstrate the activation of LFP by FLGO, the presence of any other carbonaceous additive in the composites was avoided. The prepared composite was further compared to the two other LFP mixtures with multiwalled carbon nanotubes (MWCNT) and carbon black (CB) fabricated under the same conditions. The changes in the FLGO structure during electrochemical experiments were monitored separately by Raman and infrared spectroscopies. The composites were prepared by simple mixing of LFP and 10 %wt of sp^2 carbon in D.I. water or IPA, evaporated to dryness and then treated electrochemically as described earlier for aprotic electrolytes. Fig.1 of Appendix 2 shows SEM images of those composites. The effect of cycling, i.e. the increase of the chronoamperometric charge capacities of LFP/FLGO can be seen in Fig. 13 (left). The capacities exhibit dramatic increase which is reminiscent of the spontaneous cycle-dependent activation observed also by cyclic voltammetry. The maximum capacity of ~90 mAh/g is reached after 105 chronoamperometric cycles (switching between 4 and 2.7 V vs. Li/Li$^+$). Mixtures with MWCNT and carbon black shows capacities of 20 and 60 mAh/g, respectively, followed by a gradual drop of capacity. Pure LFP is not electrochemically active and thus has almost zero capacities upon cycling. Fig. 13 (right) shows the results of galvanostatic charging at 1C rate (in battery applications 1C corresponds to one hour charge or discharge of the electrode system) during progressive chronoamperometric cycling proving electrochemical activation of the composite and increase of capacities.
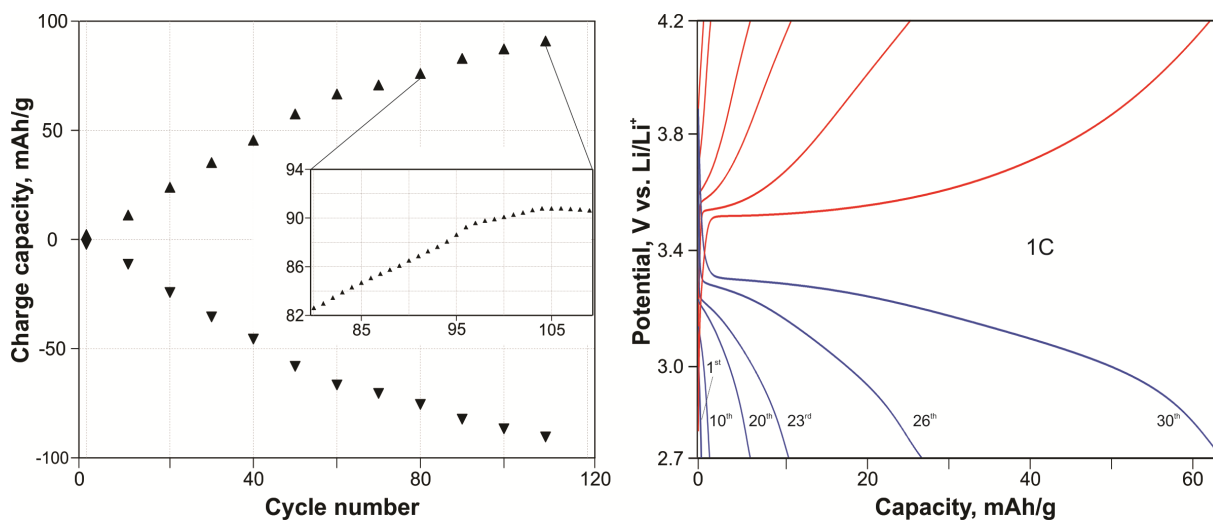
Figure 13: Anodic (4 V vs. Li/Li$^+$) and cathodic (2.7 V) capacities derived from potential-step chronoamperometric measurements of LFP with 10 wt% of added FLGO (left chart). Data for every 10th cycle are plotted. The inset zooms into the last cycles of the experiment (every cycle shown). The right chart depicts evolution of galvanostatic charge-discharge curves (1st-30th cycle).

By Raman ex-situ spectroscopy of freshly prepared and cycled electrodes, the same processes as discussed earlier for GO reduction were observed, i.e., the increase of the size of small aromatic clusters (D mode redshift), structural ordering of GO during cycling (narrowing of the D band). The behavior also confirms the explanation of the G band blueshift and I(D)/I(G) ratio increase using amorfization diagram [67] in stage two.

Fourier-transform infrared (FT-IR) spectroscopy was used as a complementary method to gain deeper insight into the changes in the FLGO structure, which occur during the electrochemical experiments. The spectra were accumulated with ZnSe anvil attenuated total reflection accessory from 320 scans. Some of the FT-IR peaks (namely at 1120, 1260, 1305, 1505 cm^{-1}) initially present vanish during the cycling (corresponding to epoxy-, carboxy- and carbonyl groups, and esters) indicating the loss of those functional groups during cycling (reduction) of FLGO. Peaks in the region of aromatic-rings-vibrations are markedly shifted, indicating changes of the graphitic structure (Fig. 14).
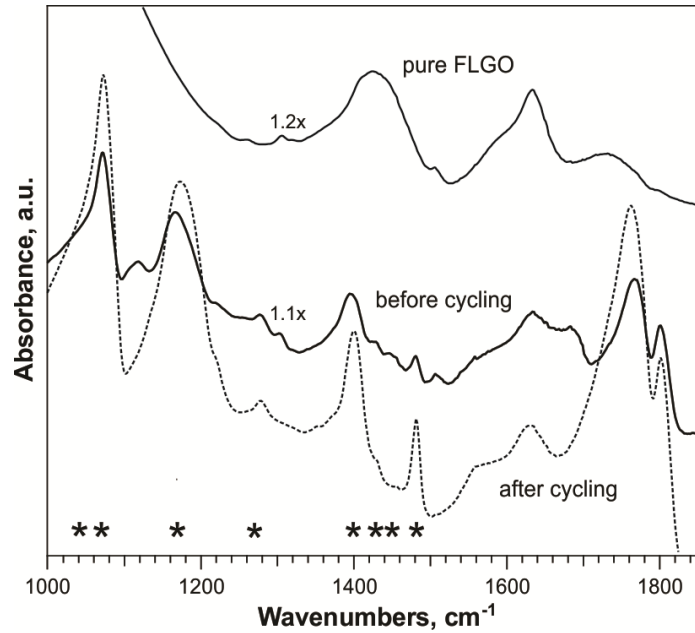
Figure 14: FT-IR spectra of pure FLGO and FLGO as the electrode material before and after electrochemical treatment. Spectra of pure FLGO and before treatment are multiplicated for clarity. PVDF binder peaks positions are marked by asterisks.

3.2 Raman in-situ monitoring of strain and doping in graphene

3.2.1 Bernal bilayer graphene under uniaxial tension

Various bilayer graphene flakes with Bernal stacking (2-L, and together with neighboring monolayer flakes, 1-L) under uniaxial strain were investigated (Appendix 3) using Raman spectroscopy (both point- and mapping-wise). The samples were prepared by mechanical cleavage and transferred on the PMMA bar (spincoated by SU-8 photoresist) and consequently covered by additional layer of polymers (PMMA or SU-8). Samples were strained using cantilever beam experimental setup (Fig. 9) and the shifts and linewidths of the Raman G and 2D bands were compared.

As was already mentioned, uniaxial strain induces G peak splitting to G^+ and G^- with shift rates about 31 and 10 cm^{-1}/% (uniaxial strain, on polymer) [90, 91]. Splitting of the 2D band was also observed in some cases, but it is strongly influenced by the excitation energy and mutual orientation of the strain, polarization direction of excitation/scattered light and

crystal lattice [79]. In the first studied case, the measured flake (F1) consists of mono- and bi-layer region with the orientation of both of ~21° with respect to the strain axis. The lattice orientation was calculated from G^+/G^- intensities. The same orientation of the lattice in both regions confirms that indeed both regions belong to the same flake [79, 90]. The strain-shift rates of both G subpeaks confirm normal (i.e. full) stress transfer behavior of both mono- and bilayer regions in spite of the twice higher stiffness of the bilayer. Evolution of the 2D subpeaks is different for monolayer and bilayer. In the first case the subpeaks shifted with rate of *ca.* -41.5 and -22.4 cm^{-1}/%. The first component became also more intense with increasing strain. The analysis of the 2D mode in bilayer graphene is more complicated, because it is already split into four components ($2D_{11}$, $2D_{12}$, $2D_{21}$ and $2D_{22}$) due to splitting of the π-bands and phonon band dispersions (more details in Appendix 3 text and Fig. 2). Those components were fitted by Lorentzian lineshapes with fixed and equal FWHMs for the analysis of spectra acquired under strain. During the loading, the $2D_{11}$ component blueshifts at a rate of -29 cm^{-1}/%, while the other three at ~ -50 cm^{-1}/%. The intensities of the components also change: the $2D_{12}$ intensity increases, while the other are slightly decreased. Comparing the intensities and shifts of the 2D subpeaks in mono- and bilayer graphene, it was suggested that the lower shift rate of the $2D_{11}$ component in 2-LG (of the principally same origin as the 2D band in 1-LG) and the increase of the neighboring $2D_{12}$ component is actually a joint effect reflecting the strain-induced splitting of the 1-LG-like $2D_{11}$ component in a way similar to the splitting of the 2D band in 1-LG (the $2D_{12}$ component then becomes a superposition of the original $2D_{12}$ and the faster-shifting component of the split $2D_{11}$ component, whereas the 'new' $2D_{11}$ is only the slower-moving subpeak).

Even though the shift rates measured in F1 indicated the same stress transfer in the 1- and 2LG, the maps of the Raman shift of the flake 2 (F2) show the difference of the stress uptake between 1-L and 2L graphene at high strain levels; the stress transfer is larger for the monolayer. By changing the laser excitation it was also observed that higher excitation energy causes progressive broadening of 2D FWHM. Here it is important to remind that 2D splitting (lineshape) depends not only on the excitation energy, but also on the polarization of light (both incident and scattered) and lattice orientation, so it is crucial to take all these terms into consideration. In the F2, all four components of the 2-L 2D band have linear strain-shift rates and linear evolution of intensities , which correlates with simple broadening of the 2D peak in the monolayer part of F2 (i.e., no observable splitting). The obvious correspondence between

the overall behavior of the $2D_{11}$ in 2-L and 2D in 1-L also in the F2 flake supports the hypothesis of relating the origin of these two peaks. Furthermore, on the F2 maps, various inhomogeneities in the strain field (at 0.74% nominal strain) were studied. Firstly, the stress transfer is negligible at the edges of the flakes as well as close to a linear defect observed in the monolayer part, consistently with the shear-lag theory [92]. Secondly, at higher nominal stress of ~0.5%, slippage or failure is presumed according to the break in the linearity of 2D components shifts. Lastly, in the small area of the bilayer, distinct Raman spectra with features different from those of AB stacked graphene were observed: the G peak in this region consist of one more intense component (1578 cm^{-1}) and one much weaker (1594 cm^{-1}), which is clearly different from G^{+} and G^{-} splitting in a 'normal' bilayer. The 2D peak has also a particular shape (no clear splitting into the 4 components), and additionally, no D band was present (hence no local defects). A lot of possible causes were taken into consideration, but this event was finally described as a creation of local asymmetry of the two graphene layers due to unequal strain fields imposed on the two layers from the top/bottom polymer. The two G subpeaks were assigned to E_g and E_u modes; the latter is normally active only in IR but here it is activated by the breaking of the bilayer inversion symmetry upon unequal deformation.

3.2.2 Stress and charge transfer in graphene under uniaxial tension

Both strain and doping influence the Raman bands in different ways, but, usually, both are present simultaneously (strain could be induced by preparation and transfer processes, doping can be involved due to substrate charges and/or impurities on the graphene surface). Vector analysis of the phase space of the G and 2D bands was successfully tested to decompose strain and doping in the presence of biaxial strain [68, 93, 94]. In the Appendix 4, simply supported or embedded CVD graphene was tested under uniaxial loading using the cantilever beam technique together with *in-situ* monitoring by Raman microspectroscopy. CVD graphene was transferred by two different methods: PDMS-assisted dry transfer technique (PIB transfer) and standard wet PMMA transfer, both described earlier. Median size of the graphene domains between cracks, folds or wrinkles is ~2 um in the PDMS-assisted transfer and less than 1 um in PMMA-assisted transfer. The domains are mostly delimited by cracks in the PDMS transfer and by wrinkles in the PMMA transfer. After

transfer to plastic PMMA bar (cleaned and spincoated with different polymers), some samples were covered by an additional layer of polymer to better fix the graphene for further mechanical experiments.

The shifts of the G and 2D bands were compared as well as widths of both bands. In this way, the level of charge transfer doping and strain can be assessed. In general, strain causes G peak softening and splitting (biaxial strain ~60 cm^{-1}/%, uniaxial 37 and 19 cm^{-1}/% for freestanding graphene, 31 and 10 cm^{-1}/% for graphene on polymer) for uniaxial strain [78, 90, 95]. Also, strain has a larger influence on 2D band, again redshift for biaxial (or simple supported uniaxial) strain by a factor ~2.2-2.5, and a factor ~3 for uniaxial strain in full supported samples [96, 97]. Those factors are calculated as an average, as for example G$^+$ (10 cm^{-1}/%), G$^-$ (31 cm^{-1}/%) and 2D (60 cm^{-1}/%) are shifts under uniaxial loading. For doping, G band is more sensitive compared to 2D band. Doping causes upshift for G and 2D peaks with a factor ~0.5-0.7 for hole injection (p-doping). When concentration of electrons is below 2 x 10^{13} cm^{-2}, the shifts are only negligible for the 2D band, and followed by a non-linear redshift [81, 98]. Doping change can be estimated by the calculation (Eq. 4) , for the case of p-doping [94].

$$\Delta\omega G = -0.986n^2 + 9.847n$$

Equation 4: Simplified formula for estimation of the hole concentration change (in order of 10^{13} cm^{-2}).
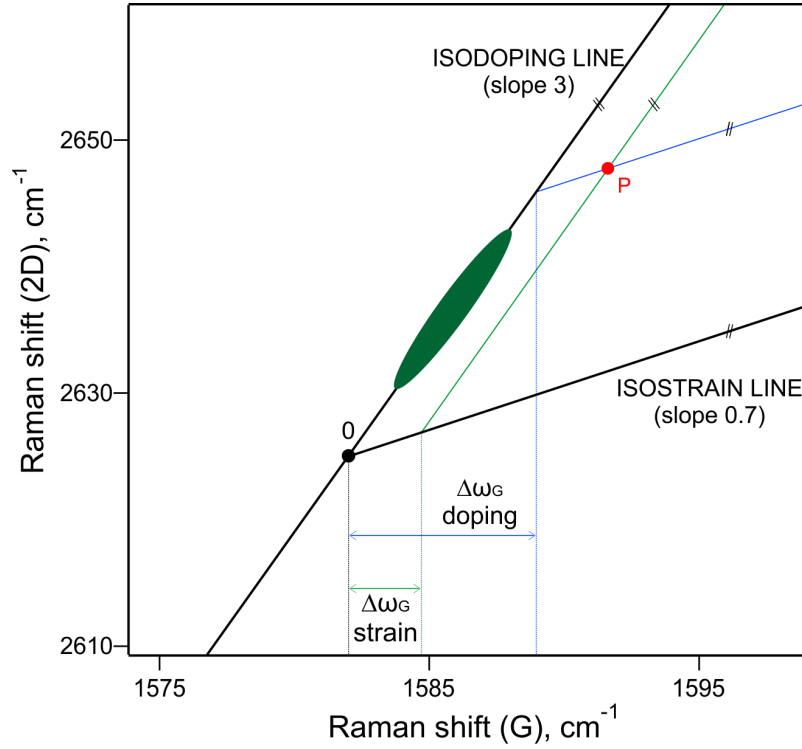
Figure 15: An example of the G-2D vector analysis of a graphene sample. P: G and 2D positions of the measured sample; 0: G and 2D zero position for freestanding graphene (no doping from substrate; 2D position depends on the excitation energy) [99]; $\Delta\omega_G$ strain: shift of the G band due to present strain; $\Delta\omega_G$ doping: shift induced by doping.

These differences in the G and 2D band shifts caused by strain/doping can be used for the vector analysis, where the data points in the orthogonal G and 2D position phase space are converted into coordinate system of doping (expressed as charge carrier concentration) and strain (expressed as relative elongation) [68]. Thus, in the vector analysis diagram (Fig. 15), different axes are used for calculating strain and doping contribution, namely iso-doping (line slope of 3 for uniaxial strain in contrast to the normally used slope of 2.2-2.4 for biaxial strain) and iso-strain (slope 0.7 for hole doping) lines. In this vector system, one can subtract strain and doping components (and therefore the doping/strain levels) from the total G (2D) shift using zero position [0;0] in which no strain or doping is present. The zero point 2D coordinate varies with laser excitation energy and it is benchmarked from freestanding graphene (i.e. zero doping) [99]. By vector analysis is also possible to estimate the distribution of doping/strain in a larger area (from Raman mapping). In Fig. 15, an example of one-point Raman measurement (red point, P), with analysis of the strain and doping

components, is showed. Also, there is a theoretical example of such an area (green oval) in the plot, where Raman parameters could have lain in the case of the graphene flake with only variation in strain present (i.e. without substantial doping).

In Appendix 4, three different cases are described in detail using the Raman spectroscopy vector analysis. First case, graphene transferred by the PIB technique additionally covered by parylene C polymer, second case, PMMA transferred graphene covered by parylene C, and third case, graphene transferred using PIB but simply supported with no after-transfer covering. In all cases, one point as well as the whole flake area was examined by Raman spectroscopy during sample bending (i.e. application of uniaxial in-plane tensile strain). Already at the first look at the plotted G and 2D band parameters in the first case, it is obvious that there are some discrepancies between theoretical and measured shift rates of both bands that would occur when only strain would take place (Fig. 3: B and C, Appendix 4). Those observations can be explained rationally by changes in the doping during the bending, which have stronger influence on the G band compared to the 2D band. Furthermore, it is known that the charge carrier concentration spatially fluctuates in graphene (the so-called charge puddles [100]), causing a wide distribution of the G Raman band shift (if the fluctuations are at a lateral scale larger than the Raman spot) or the G band broadening (if smaller) [101]. Both effects are present, therefore the strain shift rates have to be corrected taking into account the charge doping as well. The analysis of single-spot Raman measurement reveals local depletion of holes during the experiment. It can be presumed that measured spot was located inside a charge puddle with increased hole concentration. During stretching the graphene was flattened (partially), thus a better contact was made, and consequently the charge was better distributed to the surrounding graphene.
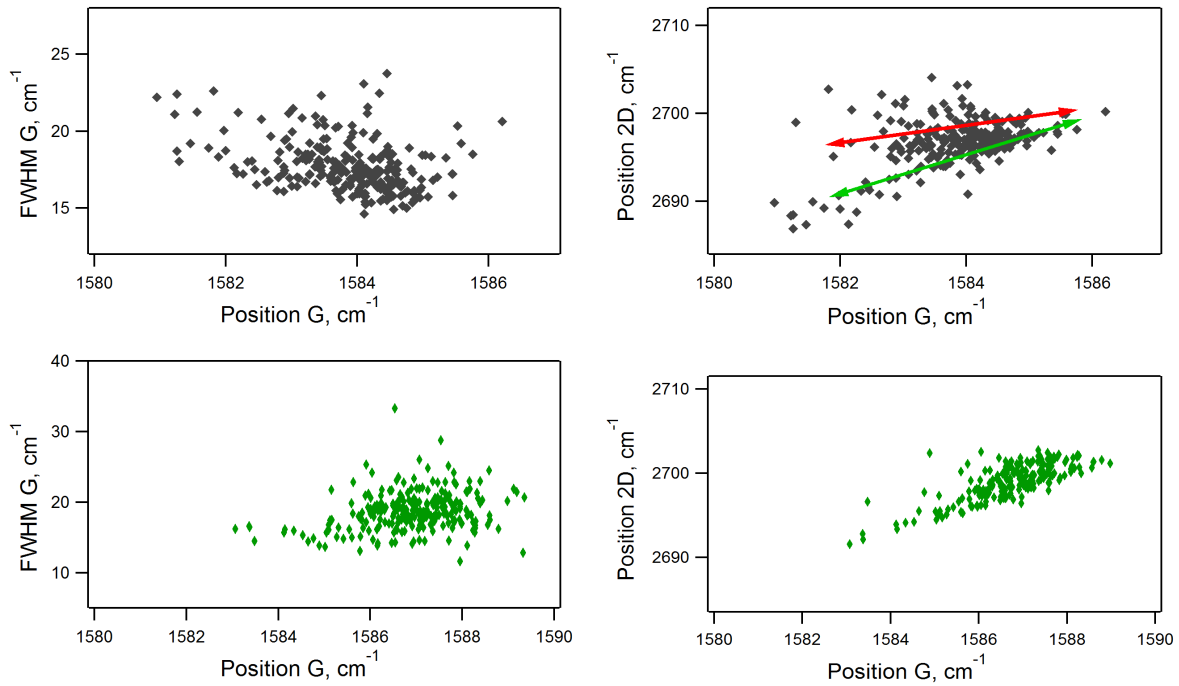
Figure 16: An example of correlations of the fitted parameters of the G and 2D bands of the graphene flake transferred on the PMMA covered substrate (black diamonds at 0% nominal strain, green diamonds at 1% nominal strain). Red and green arrows indicate theoretical directions of values' distribution caused by doping and strain (slope 0.7 and 3), respectively.

On the other hand, data from maps (0 and 0.5% of nominal strain) show different behavior. Using vector analysis on median values from the maps it was revealed that the contribution of doping to the changes is only minor (line-slope between the medians of 3.6, $\Delta n \sim 0.1 \times 10^{13}$ cm^{-2}). The G-peak shift rate is 8.9 cm^{-1}/% in this case, hence the ratio to the theoretical shift is 0.44 (i.e., the stress transfer efficiency). The vector analyses of the other two cases are discussed in detail in the attached paper. Comparing all three cases, it is obvious that the applied strain causes gradual alignment of the crumpled CVD graphene on the substrate. The flattening causes changes in carrier concentration. The strain distribution across the samples varies significantly, owing to the growth and transfer process, which induces wrinkles and faults in the CVD graphene. In simply supported specimens, the stress transfer efficiency is generally very low and the changes in Raman spectra are dominated by variations in the charge transfer originating from the realignment of the domains on the substrate upon the application of strain. In contrast, samples covered with an additional

polymer layer reveal profoundly increased stress transfer efficiencies, and the changes of charge doping levels are negligible. Vector analysis of the one single spot can be deceptive and the processes in whole flake can vary noticeably, thus data obtained from whole flake maps should be assessed instead. Additionally, this method can be used for evaluation of the strain/doping variation inside one sample where wrinkles, folds and cracks can induce spatial strain/doping variations.

3.3 Development of a new method for in-situ Raman (micro)-spectroelectrochemistry

The previous chapters show clearly that the process of strain and charge transfer doping occur simultaneously and, very often, they influence each other in the studied specimens. Hence, the idea of incorporation of both (electrochemical and mechanical) techniques into one in-situ spectroscopic set-up is particularly appealing to gain new insights of the mutual relation between crystal and electronic structure of 2D materials. The combination of the bending method and in-situ Raman SECH meets in the making of a new apparatus. Scheme of the basic instrumental setup of it is depicted in Fig. 17.

The method consists of a cantilever beam bending device, μ-droplet electrochemical system and Raman spectrometer with 'free-space' microscope to accommodate the bulky in-situ measuring setup. The electrochemistry is conducted in a droplet (of average diameter ~X-X0 μm) substituting the classic electrochemical cell. The droplet itself contains an electrolyte solution (6M KCl, the high concentration to avoid fast evaporation; it also allows to overcome the high resistance in the confined system) as well as the microcapillary does (apex diameter of few μm), which is inserted inside the droplet and contains electrodes (RE: Ag/AgCl, CE: Pt). The graphene, or other 2D crystal, contacted by a silver paste serves as a working electrode. Part of the system is mounted on the piezo-driven micro-manipulating device and connected to the micro-pump enabling the control of the droplet shape, diameter and volume. The droplet additionally works as a lens for the laser beam and enhances the signal slightly when optimally focused. Controlled doping (shift of the Fermi level) and strain level (breaking the lattice symmetry, changing the chemical potential) can thus be studied on a microscale. By an electrochemical polarization and by bending of the sample, it is possible

to determine the real zero level of Raman shifts for strain and doping when both are already present in the freshly made samples (common situation). This experimental setup also allows to control/measure the strain and the doping independently.
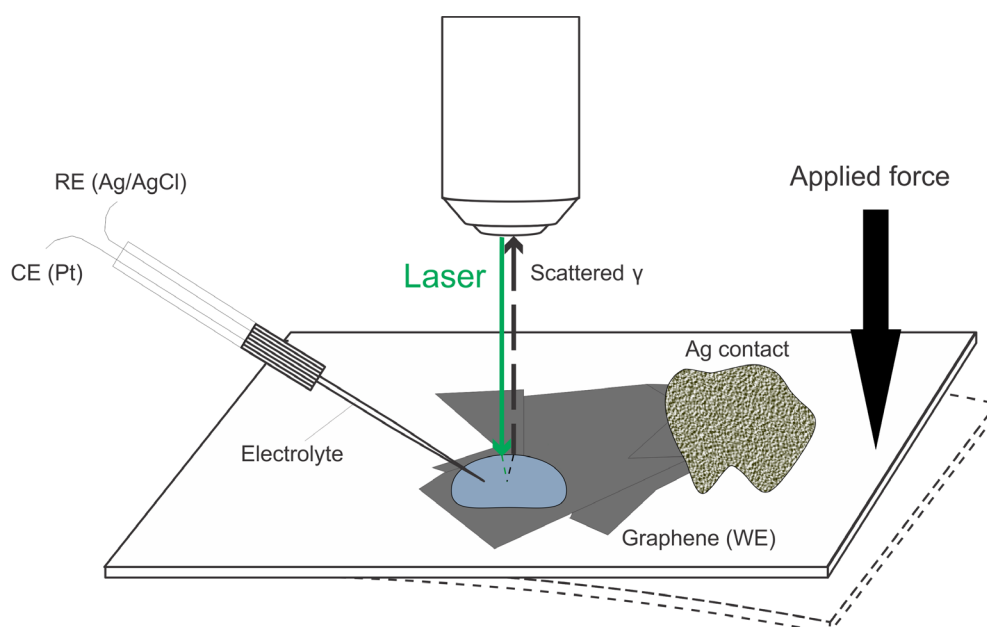
Figure 17: In-situ uniaxial deformation combined with μ-droplet Raman spectroelectrochemistry.

The μ-droplet setup was already tested on two different graphene samples, one on the bare PMMA polymer beam and one on the SU-8 resist covering the beam. The first one showed a larger initial charge doping ($E_F \sim$ -0.32 eV), as determined from the minima in the evolution of the Raman G band with the applied both negative and positive potentials, but smaller stress transfer efficiency (~25%), as obtained from analysis of G and 2D band shifts compared to the existing benchmarks. The second sample showed a negligible initial charge doping ($E_F \sim$ -0.05 eV) and a larger stress transfer efficiency (~50%).

Figure 18: Raman G (top left) and 2D band (top right) positions in a single layer graphene as a function of nominal strain (%) and potential (V vs Ag/AgCl). The real strain is ~25% of the nominal strain. The strain has been changed in 0.2% steps and the potential in 0.1 V steps.

4 Conclusions

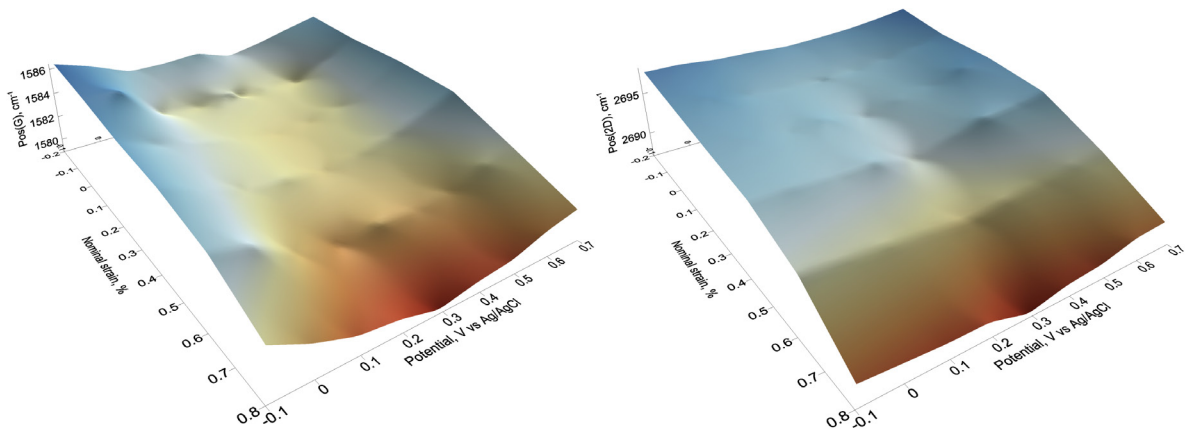Reduction of FLGO and GNP during electrochemical cycling was studied in Appendix 1. In-situ Raman spectroelectrochemistry showed that the redox processes were reversible for graphene nanoplatelets and irreversible for graphene oxide. Hence, the primary degree of oxidation has an influence on the initial reduction process, which can be described by two phases for FLGO. Raman shifts and evolution of intensities and linewidths of the single resonance tangential E_{2g} "graphitic" G mode and the defect-induced double resonance D and D' modes were examined using different fitting models. The derived data showed a great complexity of the structural changes occurring during the reduction of FLGO primarily in the first phase, with a predominant effect of narrowing of the defect distribution and probably a simultaneous increase of the stacking order of graphene sheets. Changes in the second phase were affected mostly by mild oxidation/reduction and/or by graphene lattice expansion/contraction. Furthermore, XPS measurements pointed to a preferential removal of carboxy- and hydroxy- functional groups with epoxy groups still present.

In Appendix 2, mainly nanocrystalline olivine-type $LiFePO_4$ was used as the cathode material because of its low-cost, stability and availability. To improve the conductivity and charge transfer in the active electrode material, some form of sp^2-hybridized carbon should be added. In the presented study carbon nanotubes, conductive carbon black and few-layer graphene oxide were compared as the conductive additive to olivine material. Various voltammetric and amperometric measurements were performed to investigate the influence of the carbon material on the reversibility, cycle stability and capacity of the prepared electrodes. The composite of LFP and FLGO showed an intriguing evolution of capacities during the electrochemical treatment, when the charge/discharge cycling of this nanocomposite resulted in a progressive reduction of the FLGO, which in turns lead to its better conductivity and a gradual capacity increase of the tested composite of up to 90 mAh/g. To elucidate the observed behavior, Raman and IR spectroscopy were used for the characterization of the structural changes in the graphene oxide induced by electrochemical charge/discharge processes.

In Appendix 3, a systematic Raman study of uniaxially deformed mono- and bilayer graphene samples embedded in the polymer matrix, using laser energies from the visible to the near-IR range, is presented. It was shown that the strain directly influenced the double

resonance bands, with the $2D_{11}$ component in the bilayer being more sensitive to the induced deformations, comparably to the 2D band in the monolayer. In terms of the mechanical stability, we observed that the interface failure or slippage of the bilayer occurs at lower tension levels compared to the monolayer part of the same flake and the stress transfer is zero on the edges of the flakes. Additionally, the Bernal-stacked two layers fully embedded in a matrix are locally susceptible to non-uniform strain field components, which induce a breaking of the bilayer inversion symmetry. This in turn leads to the activation of the infrared E_u mode and the appearance of a single broad 2D band.

In Appendix 4, it was shown that the strain distribution across the uniaxially loaded graphene samples varies significantly, owing to the growth and transfer process, which induces wrinkles and faults in the CVD graphene. The vector analysis method uses the correlation of the G and 2D band frequencies to separate biaxial strain from charge doping in various graphene samples and can be modified for uniaxial as well as biaxial strain applied to the graphene flakes. In simply supported specimens under uniaxial loading, the stress transfer efficiency is generally very low and the changes in Raman spectra were dominated by variations in the charge transfer originating from the realignment of the graphene domains on the substrate upon the application of strain. On the other hand, samples covered with an additional polymer layer revealed profoundly increased stress transfer efficiencies, and the changes of charge doping levels were negligible. Furthermore, it was also shown that the analysis performed on a single spot can be misleading and only large area map investigations can provide comprehensive information about the stress and doping in the graphene samples.

At the final stage of the thesis preparation, a method of "μ-droplet spectroelectrochemistry" for mechanical experiment of the 2D materials has been developed and tested in the first experiments. This technique allows, indeed, to conduct highly localized spectroelectrochemical characterization of isolated 2D crystals upon strain loading together with in-situ Raman spectroscopic investigation.

5 References

[1] K.S. Novoselov, A.K. Geim, S.V. Morozov, D. Jiang, Y. Zhang, S.V. Dubonos, I.V. Grigorieva, A.A. Firsov, Electric field effect in atomically thin carbon films, Science 306 (2004) 666-669.

[2] C. Lee, X.D. Wei, J.W. Kysar, J. Hone, Measurement of the elastic properties and intrinsic strength of monolayer graphene, Science 321 (2008) 385-388.

[3] A.A. Balandin, S. Ghosh, W.Z. Bao, I. Calizo, D. Teweldebrhan, F. Miao, C.N. Lau, Superior thermal conductivity of single-layer graphene, Nano Lett 8 (2008) 902-907.

[4] V. Carozo, C.M. Almeida, E.H.M. Ferreira, L.G. Cancado, C.A. Achete, A. Jorio, Raman Signature of Graphene Superlattices, Nano Lett 11 (2011) 4527-4534.

[5] W.T. Pong, C. Durkan, A review and outlook for an anomaly of scanning tunnelling microscopy (STM): Superlattices on graphite, J Phys D Appl Phys 38 (2005) R329-R355.

[6] A.T. N'Diaye, J. Coraux, T.N. Plasa, C. Busse, T. Michely, Structure of epitaxial graphene on Ir(111), New J Phys 10 (2008).

[7] B.C. Brodie, On the atomic weight of graphite, Philos Trans Roy Soc Lond 149 (1859) 249–259.

[8] W.S. Hummers, R.E. Offeman, Preparation of Graphitic Oxide, J Am Chem Soc 80 (1958) 1339-1339.

[9] D.A. Dikin, S. Stankovich, E.J. Zimney, R.D. Piner, G.H.B. Dommett, G. Evmenenko, S.T. Nguyen, R.S. Ruoff, Preparation and characterization of graphene oxide paper, Nature 448 (2007) 457-460.

[10] H.Y. He, J. Klinowski, M. Forster, A. Lerf, A new structural model for graphite oxide, Chem Phys Lett 287 (1998) 53-56.

[11] W. Gao, L.B. Alemany, L.J. Ci, P.M. Ajayan, New insights into the structure and reduction of graphite oxide, Nat Chem 1 (2009) 403-408.

[12] W.W. Cai, R.D. Piner, F.J. Stadermann, S. Park, M.A. Shaibat, Y. Ishii, D.X. Yang, A. Velamakanni, S.J. An, M. Stoller, J.H. An, D.M. Chen, R.S. Ruoff, Synthesis and solid-state NMR structural characterization of (13)C-labeled graphite oxide, Science 321 (2008) 1815-1817.

[13] H. Chen, M.B. Muller, K.J. Gilmore, G.G. Wallace, D. Li, Mechanically strong, electrically conductive, and biocompatible graphene paper, Adv. Mater. 20 (2008) 3557-+.

[14] C. Mattevi, G. Eda, S. Agnoli, S. Miller, K.A. Mkhoyan, O. Celik, D. Mastrogiovanni, G. Granozzi, E. Garfunkel, M. Chhowalla, Evolution of Electrical, Chemical, and Structural Properties of Transparent and Conducting Chemically Derived Graphene Thin Films, Adv Funct Mater 19 (2009) 2577-2583.

[15] H.A. Becerril, J. Mao, Z. Liu, R.M. Stoltenberg, Z. Bao, Y. Chen, Evaluation of Solution-Processed Reduced Graphene Oxide Films as Transparent Conductors, Acs Nano 2 (2008) 463-470.

[16] S. Stankovich, D.A. Dikin, R.D. Piner, K.A. Kohlhaas, A. Kleinhammes, Y. Jia, Y. Wu, S.T. Nguyen, R.S. Ruoff, Synthesis of graphene-based nanosheets via chemical reduction of exfoliated graphite oxide, Carbon 45 (2007) 1558-1565.

[17] Y. Harima, S. Setodoi, I. Imae, K. Komaguchi, Y. Ooyama, J. Ohshita, H. Mizota, J. Yano, Electrochemical reduction of graphene oxide in organic solvents, Electrochim. Acta 56 (2011) 5363-5368.

[18] J. Kauppila, P. Kunnas, P. Damlin, A. Viinikanoja, C. Kvarnström, Electrochemical reduction of graphene oxide films in aqueous and organic solutions, Electrochim. Acta 89 (2013) 84-89.

[19] W. Li, J. Liu, C. Yan, Reduced graphene oxide with tunable C/O ratio and its activity towards vanadium redox pairs for an all vanadium redox flow battery, Carbon 55 (2013) 313-320.

[20] X.-Y. Peng, X.-X. Liu, D. Diamond, K.T. Lau, Synthesis of electrochemically-reduced graphene oxide film with controllable size and thickness and its use in supercapacitor, Carbon 49 (2011) 3488-3496.

[21] G.K. Ramesha, S. Sampath, Electrochemical Reduction of Oriented Graphene Oxide Films: An in Situ Raman Spectroelectrochemical Study, J. Phys. Chem. C 113 (2009) 7985-7989.

[22] Y. Shao, J. Wang, M. Engelhard, C. Wang, Y. Lin, Facile and controllable electrochemical reduction of graphene oxide and its applications, J. Mater. Chem. 20 (2010) 743-748.

[23] H. Yu, J. He, L. Sun, S. Tanaka, B. Fugetsu, Influence of the electrochemical reduction process on the performance of graphene-based capacitors, Carbon 51 (2013) 94-101.

[24] Z. Wang, X. Zhou, J. Zhang, F. Boey, H. Zhang, Direct Electrochemical Reduction of Single-Layer Graphene Oxide and Subsequent Functionalization with Glucose Oxidase, J. Phys. Chem. C 113 (2009) 14071-14075.

[25] M. Zhou, Y. Wang, Y. Zhai, J. Zhai, W. Ren, F. Wang, S. Dong, Controlled Synthesis of Large-Area and Patterned Electrochemically Reduced Graphene Oxide Films, Chem. Eur. J. 15 (2009) 6116-6120.

[26] M. Bousa, O. Frank, I. Jirka, L. Kavan, In situ Raman spectroelectrochemistry of graphene oxide, Phys Status Solidi B 250 (2013) 2662-2667.

[27] M. Bousa, O. Frank, L. Kavan, Progressive In Situ Reduction of Graphene Oxide Studied by Raman Spectroelectrochemistry: Implications for a Spontaneous Activation of LiFePO4 (Olivine), Electroanal 26 (2014) 57-61.

[28] K.S. Novoselov, A.K. Geim, S.V. Morozov, D. Jiang, M.I. Katsnelson, I.V. Grigorieva, S.V. Dubonos, A.A. Firsov, Two-dimensional gas of massless Dirac fermions in graphene, Nature 438 (2005) 197-200.

[29] R.J. Young, I.A. Kinloch, L. Gong, K.S. Novoselov, The mechanics of graphene nanocomposites: A review, Compos Sci Technol 72 (2012) 1459-1476.

[30] P.R. Somani, S.P. Somani, M. Umeno, Planer nano-graphenes from camphor by CVD, Chem Phys Lett 430 (2006) 56-59.

[31] Z.Z. Sun, Z. Yan, J. Yao, E. Beitler, Y. Zhu, J.M. Tour, Growth of graphene from solid carbon sources, Nature 468 (2010) 549-552.

[32] X.C. Gan, H.B. Zhou, B.J. Zhu, X.Y. Yu, Y. Jia, B. Sun, M.Y. Zhang, X.J. Huang, J.H. Liu, T. Luo, A simple method to synthesize graphene at 633 K by dechlorination of hexachlorobenzene on Cu foils, Carbon 50 (2012) 306-310.

[33] J.K. Lee, S. Lee, Y.I. Kim, J.G. Kim, B.K. Min, K.I. Lee, Y. Park, P. John, The seeded growth of graphene, Sci Rep-Uk 4 (2014).

[34] P.W. Sutter, J.I. Flege, E.A. Sutter, Epitaxial graphene on ruthenium, Nat Mater 7 (2008) 406-411.

[35] G. Nandamuri, S. Roumimov, R. Solanki, Chemical vapor deposition of graphene films, Nanotechnology 21 (2010).

[36] S. Gadipelli, I. Calizo, J. Ford, G.J. Cheng, A.R.H. Walker, T. Yildirim, A highly practical route for large-area, single layer graphene from liquid carbon sources such as benzene and methanol, J Mater Chem 21 (2011) 16057-16065.

[37] R.K. Paul, S. Badhulika, S. Niyogi, R.C. Haddon, V.M. Boddu, C. Costales-Nieves, K.N. Bozhilov, A. Mulchandani, The production of oxygenated polycrystalline graphene by one-step ethanol-chemical vapor deposition, Carbon 49 (2011) 3789-3795.

[38] C. Coletti, C. Riedl, D.S. Lee, B. Krauss, L. Patthey, K. von Klitzing, J.H. Smet, U. Starke, Charge neutrality and band-gap tuning of epitaxial graphene on SiC by molecular doping, Phys Rev B 81 (2010).

[39] J. Ek-Weis, S. Costa, O. Frank, M. Kalbac, Heating Isotopically Labeled Bernal Stacked Graphene: A Raman Spectroscopy Study, J Phys Chem Lett 5 (2014) 549-554.

[40] L.X. Zhu, X. Zhao, Y.Z. Li, X.Y. Yu, C. Li, Q.H. Zhang, High-quality production of graphene by liquid-phase exfoliation of expanded graphite, Mater Chem Phys 137 (2013) 984-990.

[41] P. Blake, P.D. Brimicombe, R.R. Nair, T.J. Booth, D. Jiang, F. Schedin, L.A. Ponomarenko, S.V. Morozov, H.F. Gleeson, E.W. Hill, A.K. Geim, K.S. Novoselov, Graphene-based liquid crystal device, Nano Lett 8 (2008) 1704-1708.

[42] M. Lotya, Y. Hernandez, P.J. King, R.J. Smith, V. Nicolosi, L.S. Karlsson, F.M. Blighe, S. De, Z.M. Wang, I.T. McGovern, G.S. Duesberg, J.N. Coleman, Liquid Phase Production of Graphene by Exfoliation of Graphite in Surfactant/Water Solutions, J Am Chem Soc 131 (2009) 3611-3620.

[43] C. Berger, Z.M. Song, T.B. Li, X.B. Li, A.Y. Ogbazghi, R. Feng, Z.T. Dai, A.N. Marchenkov, E.H. Conrad, P.N. First, W.A. de Heer, Ultrathin epitaxial graphite: 2D electron gas properties and a route toward graphene-based nanoelectronics, J Phys Chem B 108 (2004) 19912-19916.

[44] H. Tanaka, R. Arima, M. Fukumori, D. Tanaka, R. Negishi, Y. Kobayashi, S. Kasai, T.K. Yamada, T. Ogawa, Method for Controlling Electrical Properties of Single-Layer Graphene Nanoribbons via Adsorbed Planar Molecular Nanoparticles (vol 5, 12341, 2015), Sci Rep-Uk 5 (2015).

[45] D.V. Kosynkin, A.L. Higginbotham, A. Sinitskii, J.R. Lomeda, A. Dimiev, B.K. Price, J.M. Tour, Longitudinal unzipping of carbon nanotubes to form graphene nanoribbons, Nature 458 (2009) 872-U875.

[46] U. Narula, C.M. Tan, C.S. Lai, Growth Mechanism for Low Temperature PVD Graphene Synthesis on Copper Using Amorphous Carbon, Sci Rep-Uk 7 (2017).

[47] K.S. Kim, Y. Zhao, H. Jang, S.Y. Lee, J.M. Kim, K.S. Kim, J.H. Ahn, P. Kim, J.Y. Choi, B.H. Hong, Large-scale pattern growth of graphene films for stretchable transparent electrodes, Nature 457 (2009) 706-710.

[48] Y. Lee, S. Bae, H. Jang, S. Jang, S.-E. Zhu, S.H. Sim, Y.I. Song, B.H. Hong, J.-H. Ahn, Wafer-Scale Synthesis and Transfer of Graphene Films, Nano Lett. 10 (2010) 490-493.

[49] M. Bousa, G. Anagnostopoulos, E. del Corro, K. Drogowska, J. Pekarek, L. Kavan, M. Kalbac, J. Parthenios, K. Papagelis, C. Galiotis, O. Frank, Stress and charge transfer in uniaxially strained CVD graphene, Phys Status Solidi B 253 (2016) 2355-2361.

[50] O. Frank, M. Bousa, I. Riaz, R. Jalil, K.S. Novoselov, G. Tsoukleri, J. Parthenios, L. Kavan, K. Papagelis, C. Galiotis, Phonon and Structural Changes in Deformed Bernal Stacked Bilayer Graphene, Nano Lett 12 (2012) 687-693.

[51] J. Song, F.-Y. Kam, R.-Q. Png, W.-L. Seah, J.-M. Zhuo, G.-K. Lim, P.K.H. Ho, L.-L. Chua, A general method for transferring graphene onto soft surfaces, Nat. Nanotechnol. 8 (2013) 356-362.

[52] M. Her, R. Beams, L. Novotny, Graphene transfer with reduced residue, Phys Lett A 377 (2013) 1455-1458.

[53] W.H. Lin, T.H. Chen, J.K. Chang, J.I. Taur, Y.Y. Lo, W.L. Lee, C.S. Chang, W.B. Su, C.I. Wu, A Direct and Polymer-Free Method for Transferring Graphene Grown by Chemical Vapor Deposition to Any Substrate, Acs Nano 8 (2014) 1784-1791.

[54] A. Capasso, M. De Francesco, E. Leoni, T. Dikonimos, F. Buonocore, L. Lancellotti, E. Bobeico, M.S. Sarto, A. Tamburrano, G. De Bellis, N. Lisi, Cyclododecane as support material for clean and facile transfer of large-area few-layer graphene, Appl Phys Lett 105 (2014).

[55] H. Li, J.M.T. Wu, X. Huang, Z.Y. Yin, J.Q. Liu, H. Zhang, A Universal, Rapid Method for Clean Transfer of Nanostructures onto Various Substrates, Acs Nano 8 (2014) 6563-6570.

[56] E. del Corro, M. Pena-Alvarez, K. Sato, A. Morales-Garcia, M. Bousa, M. Mracko, R. Kolman, B. Pacakova, L. Kavan, M. Kalbac, O. Frank, Fine tuning of optical transition energy of twisted bilayer graphene via interlayer distance modulation, Phys Rev B 95 (2017).

[57] M. Bousa, M. Kalbac, I. Jirka, L. Kavan, O. Frank, EXPERIMENTAL STUDY OF PIB-BASED CVD GRAPHENE TRANSFER EFFICIENCY, Nanocon 2015 proceeding (2015).

[58] S. Bae, H. Kim, Y. Lee, X.F. Xu, J.S. Park, Y. Zheng, J. Balakrishnan, T. Lei, H.R. Kim, Y.I. Song, Y.J. Kim, K.S. Kim, B. Ozyilmaz, J.H. Ahn, B.H. Hong, S. Iijima, Roll-to-roll production of 30-inch graphene films for transparent electrodes, Nat. Nanotechnol. 5 (2010) 574-578.

[59] L.G.P. Martins, Y. Song, T.Y. Zeng, M.S. Dresselhaus, J. Kong, P.T. Araujo, Direct transfer of graphene onto flexible substrates, P Natl Acad Sci USA 110 (2013) 17762-17767.

[60] T. Hallam, C. Wirtz, G.S. Duesberg, Polymer-assisted transfer printing of graphene composite films, Phys Status Solidi B 250 (2013) 2668-2671.

[61] C. Riedl, C. Coletti, U. Starke, Structural and electronic properties of epitaxial graphene on SiC(0 0 0 1): a review of growth, characterization, transfer doping and hydrogen intercalation, J Phys D Appl Phys 43 (2010).

[62] M. Orlita, C. Faugeras, P. Plochocka, P. Neugebauer, G. Martinez, D.K. Maude, A.L. Barra, M. Sprinkle, C. Berger, W.A. de Heer, M. Potemski, Approaching the Dirac Point in High-Mobility Multilayer Epitaxial Graphene, Phys Rev Lett 101 (2008).

[63] R. Saito, M. Hofmann, G. Dresselhaus, A. Jorio, M.S. Dresselhaus, Raman spectroscopy of graphene and carbon nanotubes, Adv Phys 60 (2011) 413-550.

[64] L.M. Malard, M.A. Pimenta, G. Dresselhaus, M.S. Dresselhaus, Raman spectroscopy in graphene, Phys Rep 473 (2009) 51-87.

[65] A.C. Ferrari, D.M. Basko, Raman spectroscopy as a versatile tool for studying the properties of graphene, Nat Nanotechnol 8 (2013) 235-246.

[66] A.C. Ferrari, Raman spectroscopy of graphene and graphite: Disorder, electron-phonon coupling, doping and nonadiabatic effects, Solid State Commun 143 (2007) 47-57.

[67] A.C. Ferrari, J. Robertson, Interpretation of Raman spectra of disordered and amorphous carbon, Phys Rev B 61 (2000) 14095-14107.

[68] J.E. Lee, G. Ahn, J. Shim, Y.S. Lee, S. Ryu, Optical separation of mechanical strain from charge doping in graphene, Nat Commun 3 (2012).

[69] M. Kalbac, H. Farhat, J. Kong, P. Janda, L. Kavan, M.S. Dresselhaus, Raman Spectroscopy and in Situ Raman Spectroelectrochemistry of Bilayer C-12/C-13 Graphene, Nano Lett 11 (2011) 1957-1963.

[70] M. Lazzeri, C. Attaccalite, L. Wirtz, F. Mauri, Impact of the electron-electron correlation on phonon dispersion: Failure of LDA and GGA DFT functionals in graphene and graphite, Phys Rev B 78 (2008).

[71] F. Tuinstra, J.L. Koenig, Raman Spectrum of Graphite, J Chem Phys 53 (1970) 1126-&.

[72] P. Venezuela, M. Lazzeri, F. Mauri, Theory of double-resonant Raman spectra in graphene: Intensity and line shape of defect-induced and two-phonon bands, Phys Rev B 84 (2011).

[73] E. del Corro, L. Kavan, M. Kalbac, O. Frank, Strain Assessment in Graphene Through the Raman 2D ' Mode, J Phys Chem C 119 (2015) 25651-25656.

[74] K. Nakada, M. Fujita, G. Dresselhaus, M.S. Dresselhaus, Edge state in graphene ribbons: Nanometer size effect and edge shape dependence, Phys Rev B 54 (1996) 17954-17961.

[75] P. Shemella, S.K. Nayak, Electronic structure and band-gap modulation of graphene via substrate surface chemistry, Appl Phys Lett 94 (2009).

[76] G. Cocco, E. Cadelano, L. Colombo, Gap opening in graphene by shear strain, Phys Rev B 81 (2010).

[77] N. Mounet, N. Marzari, First-principles determination of the structural, vibrational and thermodynamic properties of diamond, graphite, and derivatives, Phys Rev B 71 (2005).

[78] O. Frank, G. Tsoukleri, J. Parthenios, K. Papagelis, I. Riaz, R. Jalil, K.S. Novoselov, C. Galiotis, Compression Behavior of Single-Layer Graphenes, Acs Nano 4 (2010) 3131-3138.

[79] O. Frank, M. Mohr, J. Maultzsch, C. Thomsen, I. Riaz, R. Jalil, K.S. Novoselov, G. Tsoukleri, J. Parthenios, K. Papagelis, L. Kavan, C. Galiotis, Raman 2D-Band Splitting in Graphene: Theory and Experiment, Acs Nano 5 (2011) 2231-2239.

[80] F. Ding, H.X. Ji, Y.H. Chen, A. Herklotz, K. Dorr, Y.F. Mei, A. Rastelli, O.G. Schmidt, Stretchable Graphene: A Close Look at Fundamental Parameters through Biaxial Straining, Nano Lett 10 (2010) 3453-3458.

[81] A. Das, S. Pisana, B. Chakraborty, S. Piscanec, S.K. Saha, U.V. Waghmare, K.S. Novoselov, H.R. Krishnamurthy, A.K. Geim, A.C. Ferrari, A.K. Sood, Monitoring dopants by Raman scattering in an electrochemically top-gated graphene transistor, Nat Nanotechnol 3 (2008) 210-215.

[82] D.M. Basko, S. Piscanec, A.C. Ferrari, Electron-electron interactions and doping dependence of the two-phonon Raman intensity in graphene, Phys Rev B 80 (2009).

[83] J.B. Goodenough, K.S. Park, The Li-Ion Rechargeable Battery: A Perspective, J Am Chem Soc 135 (2013) 1167-1176.

[84] B. Scrosati, J. Garche, Lithium batteries: Status, prospects and future, J Power Sources 195 (2010) 2419-2430.

[85] A.S. Andersson, J.O. Thomas, The source of first-cycle capacity loss in LiFePO4, J Power Sources 97-8 (2001) 498-502.

[86] W.J. Zhang, Structure and performance of LiFePO4 cathode materials: A review, J Power Sources 196 (2011) 2962-2970.

[87] L. Kavan, R. Bacsa, M. Tunckol, P. Serp, S.M. Zakeeruddin, F. Le Formal, M. Zukalova, M. Graetzel, Multi-walled carbon nanotubes functionalized by carboxylic groups: Activation of TiO2 (anatase) and phosphate olivines (LiMnPO4; LiFePO4) for electrochemical Li-storage, J Power Sources 195 (2010) 5360-5369.

[88] L. Wang, H.B. Wang, Z.H. Liu, C. Xiao, S.M. Dong, P.X. Han, Z.Y. Zhang, X.Y. Zhang, C.F. Bi, G.L. Cui, A facile method of preparing mixed conducting LiFePO4/graphene composites for lithium-ion batteries, Solid State Ionics 181 (2010) 1685-1689.

[89] E.H. Hasdeo, A.R.T. Nugraha, M.S. Dresselhaus, R. Saito, Breit-Wigner-Fano line shapes in Raman spectra of graphene, Phys Rev B 90 (2014).

[90] T.M.G. Mohiuddin, A. Lombardo, R.R. Nair, A. Bonetti, G. Savini, R. Jalil, N. Bonini, D.M. Basko, C. Galiotis, N. Marzari, K.S. Novoselov, A.K. Geim, A.C. Ferrari, Uniaxial strain in graphene by Raman spectroscopy: G peak splitting, Gruneisen parameters, and sample orientation, Phys Rev B 79 (2009).

[91] C. Galiotis, O. Frank, E.N. Koukaras, D. Sfyris, Graphene Mechanics: Current Status and Perspectives, Annu Rev Chem Biomol 6 (2015) 121-140.

[92] L. Gong, I.A. Kinloch, R.J. Young, I. Riaz, R. Jalil, K.S. Novoselov, Interfacial Stress Transfer in a Graphene Monolayer Nanocomposite, Adv Mater 22 (2010) 2694-+.

[93] F. Fromm, P. Wehrfritz, M. Hundhausen, T. Seyller, Looking behind the scenes: Raman spectroscopy of top-gated epitaxial graphene through the substrate, New J Phys 15 (2013).

[94] O. Frank, J. Vejpravova, V. Holy, L. Kavan, M. Kalbac, Interaction between graphene and copper substrate: The role of lattice orientation, Carbon 68 (2014) 440-451.

[95] I. Polyzos, M. Bianchi, L. Rizzi, E.N. Koukaras, J. Parthenios, K. Papagelis, R. Sordan, C. Galiotis, Suspended monolayer graphene under true uniaxial deformation, Nanoscale 7 (2015) 13033-13042.

[96] C. Androulidakis, E.N. Koukaras, J. Parthenios, G. Kalosakas, K. Papagelis, C. Galiotis, Graphene flakes under controlled biaxial deformation, Sci Rep-Uk 5 (2015).

[97] J. Zabel, R.R. Nair, A. Ott, T. Georgiou, A.K. Geim, K.S. Novoselov, C. Casiraghi, Raman Spectroscopy of Graphene and Bilayer under Biaxial Strain: Bubbles and Balloons, Nano Lett 12 (2012) 617-621.

[98] M. Kalbac, A. Reina-Cecco, H. Farhat, J. Kong, L. Kavan, M.S. Dresselhaus, The Influence of Strong Electron and Hole Doping on the Raman Intensity of Chemical Vapor-Deposition Graphene, Acs Nano 4 (2010) 6055-6063.

[99] S. Berciaud, X.L. Li, H. Htoon, L.E. Brus, S.K. Doorn, T.F. Heinz, Intrinsic Line Shape of the Raman 2D-Mode in Freestanding Graphene Monolayers, Nano Lett 13 (2013) 3517-3523.

[100] R. Jalilian, L.A. Jauregui, G. Lopez, J.F. Tian, C. Roecker, M.M. Yazdanpanah, R.W. Cohn, I. Jovanovic, Y.P. Chen, Scanning gate microscopy on graphene: charge inhomogeneity and extrinsic doping, Nanotechnology 22 (2011).

[101] C. Neumann, S. Reichardt, P. Venezuela, M. Drogeler, L. Banszerus, M. Schmitz, K. Watanabe, T. Taniguchi, F. Mauri, B. Beschoten, S.V. Rotkin, C. Stampfer, Raman spectroscopy as probe of nanometre-scale strain variations in graphene, Nat Commun 6 (2015).

6 Complete list of journal publications

1) Bousa M., Laskova B., Zukalova M., Prochazka J., Chou A., Kavan., "Polycrystalline TiO_2 Anatase with a Large Proportion of Crystal Facets (001): Lithium Insertion Electrochemistry", *Journal of Electrochemical Society*, **2010**, 157, A1108-A1112.

2) Frank O., Bousa M., Riaz I., Jalil R., Novoselov K.S., Tsoukleri G., Parthenios J., Kavan L., Papagelis K., Galiotis C., "Phonon and Structural Changes in Deformed Bernal Stacked Bilayer Graphene", *NanoLetters*, **2012**, 12 (2), 687-693.

3) Bousa M., Frank O., Jirka I., Kavan L., "In situ Raman spectroelectrochemistry of graphene oxide", *Physica Status Solidi (b)*, **2013**, 250, 2662-2667.

4) Laskova B., Frank O., Zukalova M., Bousa M., Dracinsky M., Kavan L., "Lithium Insertion into Titanium Dioxide (Anatase): A Raman Study with $^{16/18}O$ and $^{6\backslash 7}Li$ Isotope Labeling", *Chemistry of Materials*, **2013**, 25, 3710−3717.

5) Bousa M., Frank O., Kavan L., "Progressive In Situ Reduction of Graphene Oxide Studied by Raman Spectroelectrochemistry: Implications for a Spontaneous Activation of $LiFePO_4$ (Olivine)", *Electroanalysis*, **2014**, 26, 57-61.

6) Hykrdova L., Bousa M., Jirkovsky J., "Intentional Hydrophilization of Aromatic Hydrocarbon Model Compounds: A Theoretical Study", *Graphene*, **2014**, 2, 101-112.

7) Laskova B., Zukalova M., Zukal A., Bousa M., Kavan L., "Capacitive contribution to Li-storage in TiO_2 (B) and TiO_2 (anatase)", *Journal of Power Sources*, **2014**, 246, 103-109.

8) Zukalova M., Bousa M., Bastl Z., Jirka I., Kavan L., "Electrochemical Doping of Compact TiO_2 Thin Layers", *Journal of Physical Chemistry C*, **2014**, 45, 25970-25977.

9) Bousa M., Anagnostopoulos G., del Corro E., Drogowska K., Pekarek J., Kavan L., Kalbac M., Parthenios J., Papagelis K., Galiotis C., Frank O., "Stress and charge transfer in uniaxially strained CVD graphene", *Physica Status Solidi (b)*, **2016**, 1-7.

10) Civis S., Bousa M., Zukal A., Knizek A., Kubelik P., Rojik P., Novakova J., Ferus M., "Spontaneous Oxygen Isotope Exchange between Carbon Dioxide and Oxygen-Containing Minerals: Do the Minerals "Breathe" CO_2?", *Journal of Physical Chemistry. C*, **2016**, 120, 508-516.

11) Del Corro E., Pena-Alvarez M., Sato K., Morales-Garcia A., Bousa M., Mracko M., Kolman R., Pacakova B., Kavan L., Kalbac M., Frank O., "Fine tuning of optical transition energy of twisted bilayer graphene via interlayer distance modulation", *Physical Review B*, **2017**, 95 (8).

12) Hajkova Z., Ledinsky M., Vetushka A., Stuchlik J., Muller M., Fejfar A., Bousa M., Kalbac M., Frank O., "Photovoltaic characterization of graphene/silicon Schottky junctions from local and macroscopic perspectives", *Chemical Physics Letters*, **2017**, 676, 82-88.

13) Jirka I., Vandrovcova M., Plsek J., Bousa M., Brabec L., Dragounova H., Bacakova L., "Interaction of human osteoblast-like Saos-2 cells with stainless steel coated by silicalite-1 films", *Material Science and Engeneering: C*, **2017**, 76, 775-781.

14) Jirka I., Vandrovcova M., Plsek J.,Bousa M., Bacakova L., "Interaction of silicalite-1 film with human osteoblast-like Saos-2 cells: The role of micro-morphology", *Materials Letters*, **2017**, 190, 229-231.

Submitted papers

15) Pacakova B., Verhagen T., Bousa M., Hubner U., Vejpravova J., Kalbac M., Frank O., "Mastering the wrinkling of self-supported graphene", *Scientific Reports*, **2017**, **submitted**.

16) Verhagen T., Pacakova B., Vales V., Drogowska K., Bousa M., Hubner U., Kalbac M., Vejpravova J., Frank O., "Tuning the interlayer interaction of a twisted multilayer wrinkle with temperature", *Physica Status Solidi (b),* **2017**, **submitted**.

6.1 Conference proceedings

1) Del Corro E., Pena-Alvarez M., Morales-Garsia A., Bousa M., Rahova J., Kavan L., Kalbac M., Frank O., "Experimental Study of PIB-based CVD Graphene Transfer Efficiency", Proceedings of *Nanocon 2015*, **2015**.

2) Bousa M., Kalbac M., Jirka I., Kavan L., Frank O., "Experimental and Theoretical Comparative Study of Monolayer and Bulk MoS$_2$ under Compression", Proceedings of *Nanocon 2015*, **2015**.

7 Abbreviations

1-L, 2-L	monolayer, bilayer
BWF	Breit-Wigner-Fano lineshape
BZ	Brillouin zone
CB	carbon black
CDD	cyclododecane
CE	counter electrode
CV	cyclic voltammetry, cyclic voltammogram
CVD	chemical vapor deposition
CHA	chronoamperometry
EC/DMC	ethylene carbonate + dimethyl carbonate
FLGO	few-layered graphene oxide
FT-IR	Fourier transform infrared spectroscopy
FWHM	full width at half-maxima
GNP	graphene nanoplatelets
GO	graphene oxide
HOPG	highly oriented pyrolytic graphite
LFP	$LiFePO_4$
MWCNT	multi-walled carbon nanotubes
NMP	*N*-methyl-2-pyrrolidone
PDMS	poly(dimethylsiloxane)
PIB	polyisobutylene
PLLA (PLA)	polylactic acid
PMMA	poly(methyl methacrylate)
PVDF	polyvinylidene fluoride
RE	reference electrode

RGO (rGO)	reduced graphene oxide
RP	Raman process
SECH	spectroelectrochemistry
SEM	scanning electron microscopy
WE	working electrode
XPS	X-ray photoelectron spectroscopy

8 List of Appendices

1) Bousa M., Frank O., Jirka I., Kavan L., „In situ Raman spectroelectrochemistry of graphene oxide", *Physica Status Solidi (b),* **2013**, 26, 57-61.

2) Bousa M., Frank O., Kavan L., „Progressive In Situ Reduction of Graphene Oxide Studied by Raman Spectroelectrochemistry: Implications for a Spontaneous Activation of LiFePO$_4$ (Olivine)", *Electroanalysis*, **2014**, 250, 2662-2667.

3) Frank, O., Bousa, M., Riaz, I., Novoselov, K. S., Tsoukleri, G., Parthenios, J., Kavan, L., Papagelis, K., Galiotis, C., „Phonon and structural changes in deformed bernal stacked bilayer graphene", *Nano Letters*, **2012**, 12, 2, 687-693.

4) Bousa M., Anagnostopoulos G., del Corro E., Drogowska K., Pekarek J., Kavan L., Kalbac M., Parthenios J., Papagelis K., Galiotis C., Frank O., „Stress and charge transfer in uniaxially strained CVD graphene", *Physica Status Solidi (b)*, **2016**, 1-7.

8.1 Appendix 1

Bousa M., Frank O., Jirka I., Kavan L., „In situ Raman spectroelectrochemistry of graphene oxide", *Physica Status Solidi (b),* **2013**, 26, 57-61.

8.2 Appendix 2

Bousa M., Frank O., Kavan L., „Progressive In Situ Reduction of Graphene Oxide Studied by Raman Spectroelectrochemistry: Implications for a Spontaneous Activation of LiFePO$_4$ (Olivine)", *Electroanalysis*, **2014**, 250, 2662-2667.

8.3 Appendix 3

Frank, O., Bousa, M., Riaz, I., Novoselov, K. S., Tsoukleri, G., Parthenios, J., Kavan, L., Papagelis, K., Galiotis, C.,, „Phonon and structural changes in deformed bernal stacked bilayer graphene", *Nano Letters*, **2012**, 12, 2, 687-693.

8.4 Appendix 4

Bousa M., Anagnostopoulos G., del Corro E., Drogowska K., Pekarek J., Kavan L., Kalbac M., Parthenios J., Papagelis K., Galiotis C., Frank O., „Stress and charge transfer in uniaxially strained CVD graphene", *Physica Status Solidi (b)*, **2016**, 1-7.